

An experimental and numerical dynamic study of thick sandwich beams using a mixed {3,2}-RZT formulation

Original

An experimental and numerical dynamic study of thick sandwich beams using a mixed {3,2}-RZT formulation / Sorrenti, Matteo; Gherlone, Marco. - In: FINITE ELEMENTS IN ANALYSIS AND DESIGN. - ISSN 0168-874X. - ELETTRONICO. - 251:(2025). [10.1016/j.finel.2025.104435]

Availability:

This version is available at: 11583/3002526 since: 2025-08-25T06:48:40Z

Publisher:

Elsevier

Published

DOI:10.1016/j.finel.2025.104435

Terms of use:

This article is made available under terms and conditions as specified in the corresponding bibliographic description in the repository

Publisher copyright

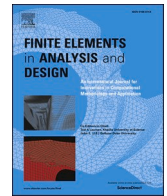
(Article begins on next page)



ELSEVIER

Contents lists available at ScienceDirect

Finite Elements in Analysis & Design

journal homepage: www.elsevier.com/locate/finel

An experimental and numerical dynamic study of thick sandwich beams using a mixed {3,2}-RZT formulation

Matteo Sorrenti ^{*} , Marco Gherlone

Department of Mechanical and Aerospace Engineering, Politecnico di Torino, Corso Duca degli Abruzzi 24, 10129, Turin, Italy

ARTICLE INFO

Keywords:

Experimental modal analysis
LASER Doppler Vibrometry
Sandwich
Mixed-refined zigzag theory
Transverse deformability
Hellinger-reissner

ABSTRACT

This work presents some numerical and experimental validations of the free-vibration behaviour of thick sandwich beams using the mixed {3,2}-Refined Zigzag Theory ($RZT_{\{3,2\}}^{(m)}$). The $RZT_{\{3,2\}}^{(m)}$ formulation enhances the Timoshenko's kinematics with a piece-wise zigzag cubic distribution of the axial displacement, and a smoothed parabolic variation for the transverse deflection. Simultaneously, an a-priori assumption is made for the transverse normal stress and the transverse shear one: the former is assumed to be a third-order power series expansion of the thickness coordinate, while the latter is derived through the integration of Cauchy's equations. The equations of motion and consistent boundary conditions for the free-vibration problem are derived through the Hellinger-Reissner (HR) theorem. Taking advantage of the C^0 -continuity requirement in the mixed governing functional, a simple two-node beam finite element (FE) is formulated, i.e., the $2B - RZT_{\{3,2\}}^{(m)}$ element. The analytical and FE performances of the proposed $RZT_{\{3,2\}}^{(m)}$ model are first addressed by means of a comparison with high-fidelity 3D FE models. Subsequently, an experimental campaign is conducted using LASER Doppler Vibrometry (LDV) to evaluate the modal parameters of a series of thick sandwich beams made of aluminium alloy face-sheets and Rohacell® WF110 core. The experimental results concerning the natural frequencies and modal shapes of the thick sandwich beam specimens under free-free boundary conditions are compared with those given by $RZT_{\{3,2\}}^{(m)}$ and high-fidelity 3D FE models. The numerical-experimental assessment highlights the effect of core and face-sheet thickness on frequency estimations, as well as the complexity of reproducing in the numerical model the experimental uncertainties. In general, the $2B - RZT_{\{3,2\}}^{(m)}$ element formulation demonstrates its accuracy and computational advantages in the dynamic analysis of thick sandwich beams.

1. Introduction

Sandwich beams are widely adopted in various engineering fields, such as aerospace, marine, civil, etc., due to their advantageous structural properties. They typically consist of two thin face-sheets bonded together with a lightweight core. This configuration exhibits excellent advantages, such as high-strength and high-stiffness, low weight, impact resistance and energy absorption, and good thermal and acoustic insulation properties [1]. However, the presence in the sandwich lay-up of various materials with different

* Corresponding author.

E-mail address: matteo.sorrenti@polito.it (M. Sorrenti).

<https://doi.org/10.1016/j.finel.2025.104435>

Received 27 May 2025; Received in revised form 29 July 2025; Accepted 18 August 2025

0168-874X/© 2025 The Authors. Published by Elsevier B.V. This is an open access article under the CC BY license (<http://creativecommons.org/licenses/by/4.0/>).

mechanical properties often results in a more pronounced transverse shear deformability and, in the case of thicker structures, a non-negligible transverse normal deformability [2]. The correct evaluation of the transverse anisotropy is necessary to guarantee better estimation of the damage mechanism that might occur, such as delamination, debonding, core crushing, etc. Researchers and engineers need to take into account these aspects in the design phase in order to correctly predict the dynamic structural response.

In the current literature, different numerical approaches are available to determine the dynamic response of sandwich beams [3,4]. For instance, analytical solutions of the three-dimensional elasticity are often used, such as Pagano [5] and Brischetto [6], but only for a few cases of lamination schemes and boundary conditions, not always representative of real applications. Alternatively, high-fidelity three-dimensional (3D) Finite Element (FE) models can provide accurate solutions but with a considerable computational cost, especially for complex geometries and sandwich stacking sequences. However, these methodologies can be exploited to validate approximated beam models used to describe the sandwich structure's behaviour.

In the current framework of mechanical analysis of sandwich structures, different models have been developed to approximate the structural response. The Equivalent Single Layer (ESL) models assume the displacement field for the whole beam thickness as a combination of functions of the thickness coordinate multiplied by a few kinematic unknowns. Among them, the most widely used are the Bernoulli-Euler beam model, the Timoshenko's Beam Theory (TBT) and the Reddy's Third-order Shear Deformation Theory (TSDT) [7], which have been extensively applied to model the behaviour of complex laminated beams, including also Functionally Graded (FG) and Carbon Nanotube (CNT) reinforced structures. As recent examples of the versatility of the ESL theories for the analysis of complex structures, we can mention the works of Hilali et al. [8,9], where the Timoshenko's kinematics has been applied for the thermal buckling analysis of sandwich-like FG beams, and the studies of Zghal et al. [10–12], where a third-order kinematics has been used to investigate the elastodynamic and stability problem of FG-CNT reinforced shell structures. With a specific focus on sandwich structures, some historical ESL-based models are worth of mentioning: the Hoff's model [13], originally developed for the bending and buckling analysis of sandwich columns; the models of Kerwin [14], DiTaranto [15], Mead and Markus [16] that aimed to develop enhanced models for damped vibration analysis of sandwich beams with viscoelastic layers; and the Higher-order Sandwich Panel Theory (HSAPT) by Frostig et al. [17], formulated for sandwich plates with transversely flexible cores. Although these examples are not exhaustive, the interested reader is referred to Refs. [18,19] for a more detailed and broader discussion of this topic.

Generally, these models are often accurate to predict global quantities such as natural frequencies, maximum displacements, and buckling loads, but they become inaccurate for thick beams and for heterogeneous lamination schemes. An alternative is offered by Layer-Wise (LW) models [20], which assume a layer-by-layer independent displacement field governed by an arbitrary number of kinematic variables. These models result in a more realistic representation of the three-dimensional response of the sandwich beam, but when the number of layers increases, the computational cost increases too.

Starting from the early 1980s, ZigZag Theories (ZZTs) have emerged, representing a good compromise between the accuracy achieved by LW models and the computational advantages of ESL ones. Generally, the displacement field in a ZZT can be assumed as the superposition of two main contributions: a global one, able to describe the general beam behaviour (as in an ESL model), and a local layer-wise refinement of the axial displacement capable of predicting the effects due to transverse anisotropy. This latter contribution is characterized by an appropriate set of "zigzag functions" that can be formulated in different ways. In Di Sciuva's original ZZT model [21], the zigzag functions are piece-wise linear functions of the thickness coordinate characterized by enforcing the transverse shear stress continuity at the layer interfaces. Their accuracy and computational advantages in FE formulations over the classical ESL/LW models brought the researchers to develop more complex models, including higher-order ZZT models [22,23] to address the behaviour of thicker structures.

By overcoming some limitations of the original ZZT models, e.g. C^1 -continuity requirement and shear stress inconsistencies at clamped edges, Tessler et al. [24] introduced the Refined Zigzag Theory (RZT), where the zigzag functions are formulated differently and characterized by a partial enforcement of the transverse shear stress continuity at the layer interfaces. The accuracy and computational efficiency of the RZT have been deeply investigated in recent years through numerical comparisons and experimental assessments; see, for instance, Refs. [25–31]. Other applications of RZT are in combination with the IsoGeometric Analysis (IGA) [32], the peridynamic differential operator [33], the inverse FEM for Structural Health Monitoring (SHM) [34,35], and neural networks [36, 37].

Further advancements have been recently introduced by Sorrenti and Di Sciuva [38] to broaden the range of applicability of the RZT formulation to angle-ply and highly anisotropic multilayered structures. The enhanced-Refined Zigzag Theory (en-RZT), which can be seen as a generalization of RZT [39], includes two additional zigzag functions that address, at the displacement level, the transverse shear stress coupling typically present in angle-ply multilayered structures. The en-RZT has recently demonstrated its accuracy and computational efficiency in addressing the static and dynamic response analysis of moderately thick multilayered composite and sandwich structures [40].

A drawback of most displacement-based models is that they cannot obtain an accurate through-the-thickness distribution of the transverse shear and normal stress for sandwich structures only using material constitutive relations. The usually adopted procedure is the stress-recovery, which requires integrating Cauchy's equations. This *a-posteriori* approach, which can be straightforwardly implemented in the analytical solutions, cannot be as easily extended to the finite element method. In fact, the stress-recovery procedure involves high-order derivatives of the kinematic unknowns, thus leading to the need for high-order FE shape functions or implementing FE patch procedures [41,42], increasing the overall computational costs.

An alternative approach is the mixed-field formulation, in which an additional stress field is assumed independently from the displacement one in order to enhance the stress prediction accuracy [43–46]. The additional field can be related to the displacement one by using appropriate mixed-variational statements, e.g., the Hu-Washizu or the Hellinger-Reissner (HR) Theorem [47–49]. More

recently, the HR variational principle has been successfully applied to the higher-order en-RZT, named as $RZT_{\{3,2\}}^{(m)}$, to evaluate the static behaviour of thick composite and sandwich angle-ply structures [50]. Furthermore, for the bending analysis of sandwich beams, a set of simple beam elements has been formulated and experimentally assessed for static bending problems [51].

The purpose of the present paper is to present the dynamic formulation of the $RZT_{\{3,2\}}^{(m)}$ model and its finite element formulation using the Hellinger-Reissner mixed variational statement. The analytical and discrete equations of motion, along with the consistent boundary conditions, are briefly presented. A numerical assessment is performed to highlight the capabilities and limitations of the presented formulation to address the dynamic behaviour of thick sandwich beams. Moreover, an experimental campaign has been conducted on a set of sandwich specimens to further investigate the accuracy of the proposed $RZT_{\{3,2\}}^{(m)}$ model addressing the free-vibrational problem. Numerical and experimental results are compared and finely discussed, highlighting the accuracy, the computational advantages and the limitations of the proposed approach, also taking into account some uncertainties typical of an experimental campaign. Finally, some concluding remarks are made based on the results, and possible future research perspectives are provided.

2. Mixed {3,2}-RZT model

2.1. Geometrical preliminaries and kinematics

Let us consider a multilayered sandwich beam of length L and cross-sectional area $A = b \times h$, where b is the width, and h is the total thickness. The beam points are referred to a Cartesian orthogonal reference system, i.e. $\mathbf{X} = (x_1, x_2, x_3)$, where x_1 corresponds to the beam longitudinal axis, with $x_1 \in [0, L]$, and x_3 is the transverse coordinate related to the beam thickness, as shown in Fig. 1, and $x_3 \in [-h/2, +h/2] \equiv [x_{3(B)}, x_{3(T)}]$. Let us indicate with the subscript (B) the quantities referred to the bottom surfaces/interfaces, whereas with the subscript (T) those referred to the top ones. The beam is made of N perfectly bonded layers. The thickness and width of each layer and of the whole beam are assumed to be constant along the beam axis. The superscript (k) denotes the quantities corresponding to the k th layer (with $k=1, \dots, N$), whereas the subscript (k) indicates the quantities corresponding to the k th interface, i.e., between the k th and $(k+1)$ th layer. Moreover, let be $h^{(k)} = x_{3(T)}^{(k)} - x_{3(B)}^{(k)} = x_{3(k+1)} - x_{3(k)}$ the thickness of the k th layer.

Throughout the paper, the symbol $(\cdot)_{,i} = \partial(\cdot)/\partial x_i$ stands for the derivative of a generic function (\cdot) with respect to the x_i coordinate. The symbol $\langle(\cdot)\rangle = b \sum_{k=1}^N \int_{x_{3(B)}^{(k)}}^{x_{3(T)}^{(k)}} (\cdot) dx_3$ refers to the integral of a generic quantity (\cdot) over the cross-sectional area.

According to the cylindrical bending assumptions, and by virtue of the sandwich lay-up configuration considered in this study, beam deformations are allowed only in the (x_1, x_3) plane, indicating that no displacements along x_2 are considered. With the aim of including the higher-order effects in the through-the-thickness description of the axial and transverse displacements of thick sandwich structures, the displacement field can be assumed according to the {3,2}-RZT formulation (see for more details Refs. [43,51]): the axial displacement varies cubically, and the transverse one quadratically across the thickness direction of the beam. Thus, the orthogonal components of the displacement vector for a beam read as follows:

$$\begin{aligned} U_1^{(k)}(x_1, x_3; t) &= u(x_1; t) + x_3 \theta(x_1; t) + \mu^{(k)}(x_3) \psi(x_1; t) \\ U_3(x_1, x_3; t) &= w^{(0)}(x_1; t) + x_3 w^{(1)}(x_1; t) + x_3^2 w^{(2)}(x_1; t) \end{aligned} \tag{1}$$

where, $U_1^{(k)}$ and U_3 are the displacements in x_1 and x_3 directions, respectively. The kinematic variables that appear in Eq. (1) are $u(x_1; t)$

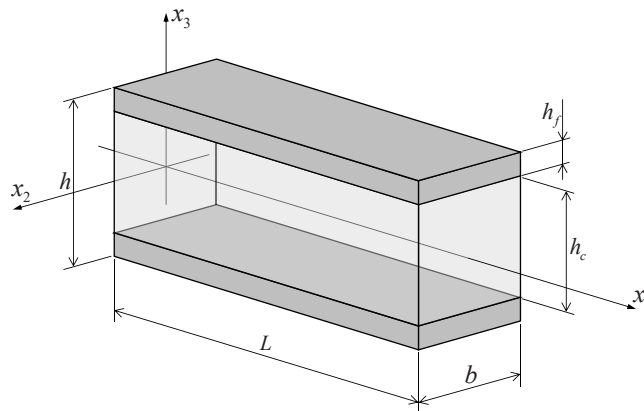


Fig. 1. Sandwich beam geometry and reference coordinate system.

and $w^{(0)}(x_1; t)$ (the uniform axial and transverse displacements), $\theta(x_1; t)$ (the average bending rotation) and $\psi(x_1; t)$ (the zigzag rotation), which are the same quantities as the linear RZT formulation [39]. Moreover, $w^{(1)}(x_1; t)$ and $w^{(2)}(x_1; t)$ are additional kinematic variables introduced in the transverse displacement component for the linear and quadratic terms, respectively. In Eq. (1), $\mu^{(k)}(x_3)$ is the third-order, piecewise continuous zigzag function whose full expression for beams reads [43,50]:

$$\mu^{(k)}(x_3) = -x_3^2\chi_0 - x_3^3\omega_0 + \varphi^{(k)}(x_3) \tag{2}$$

with

$$\begin{aligned} \omega_0 &= \frac{2(\beta^{(1)} + \beta^{(N)} + 2)}{3h^2}; \quad \chi_0 = \frac{1}{2h}(\beta^{(N)} - \beta^{(1)}); \\ \varphi^{(k)}(x_3) &= \beta^{(k)}(x_3 - x_{3(B)}) + \sum_{q=1}^{k-1} h^{(q)}(\beta^{(q)} - \beta^{(k)}) \quad (k = 1, \dots, N) \end{aligned} \tag{3}$$

$\varphi^{(k)}(x_3)$ is the linear zigzag function and $\beta^{(k)}$ is the zigzag slope of the zigzag function within the k th layer, i.e. $\beta^{(k)} = \varphi_{,3}^{(k)}$. Their values are obtained through the combination of the partial enforcement of the transverse shear stress continuity at each layer interface, and the vanishing condition of the $\mu^{(k)}(x_3)$ function at the top and bottom external beam surfaces [34,35].

Using the linear strain-displacement relations, the strain components for the beam structure read as

$$\begin{aligned} \varepsilon_{11}^{(k)}(x_1, x_3; t) &= u_{,1}(x_1; t) + x_3\theta_{,1}(x_1; t) + \mu^{(k)}(x_3)\psi_{,1}(x_1; t) \\ \varepsilon_{33}(x_1, x_3; t) &= w^{(1)}(x_1; t) + 2x_3w^{(2)}(x_1; t) \\ \gamma_{13}^{(k)}(x_1, x_3; t) &= w_{,1}^{(0)}(x_1; t) + x_3w_{,1}^{(1)}(x_1; t) + x_3^2w_{,1}^{(2)}(x_1; t) + \theta(x_1; t) + \mu_{,3}^{(k)}(x_3)\psi(x_1; t) \end{aligned} \tag{4}$$

Assuming that each layer is made of linear elastic and orthotropic material, the following beam strain-stress relations (for plane-stress condition in the (x_1, x_3) plane) are written in an appropriate mixed form [52]:

$$\begin{Bmatrix} \sigma_{11} \\ \varepsilon_{33} \\ \tau_{13} \end{Bmatrix}^{(k)} = \begin{bmatrix} E_1 & \nu_{13} & 0 \\ -\nu_{13} & S_{33} & 0 \\ 0 & 0 & G_{13} \end{bmatrix}^{(k)} \begin{Bmatrix} \varepsilon_{11} \\ \sigma_{33} \\ \gamma_{13} \end{Bmatrix}^{(k)} \tag{5}$$

where $S_{33}^{(k)} \equiv (1 - \nu_{13}^{(k)}\nu_{31}^{(k)})/E_3^{(k)}$ and $E_1^{(k)}, E_3^{(k)}, G_{13}^{(k)}, \nu_{13}^{(k)}, \nu_{31}^{(k)}$ are material mechanical properties of the k th layer.

2.2. Assumed transverse stress fields

The transverse shear and normal stress distributions obtained using the constitutive material relations are discontinuous functions across the sandwich thickness, with jumps at the interfaces. In order to enhance the {3,2}-RZT model predictivity of such stresses for thick sandwich structures and to obtain through-the-thickness continuous stresses, their distributions can be assumed independently a-priori.

Hereafter, the assumed quantities (and the quantities derived from them) are indicated with a superscript ‘‘a’’. More specifically, in this model, the transverse normal stress is assumed to be a smeared cubic function of the transverse coordinate, able to satisfy the traction conditions at the bottom and top external beam surfaces, which in the case of free-vibrations are both null (for more details, see Ref. [51]).

The transverse normal stress expression is reported here for the sake of clarity

$$\sigma_{33}^a(x_1, x_3; t) = \mathbf{P}_\sigma(x_3)\mathbf{q}_\sigma(x_1; t) \tag{6}$$

where

$$\mathbf{P}_\sigma(x_3) = \begin{bmatrix} \left(x_3^2 - \frac{h^2}{4}\right) & x_3^2 \left(x_3 - \frac{h^2}{4}\right) \end{bmatrix}; \quad \mathbf{q}_\sigma(x_1; t)^T = [\sigma_1^z(x_1; t) \quad \sigma_2^z(x_1; t)] \tag{7}$$

In Eq. (7), σ_1^z and σ_2^z are the additional stress variables introduced to approximate the transverse normal stress distributions.

The transverse shear stress is assumed a-priori to enhance the predictivity capabilities of the transverse shear deformability. Following the methodology adopted in Ref. [50], the assumed transverse shear stress distribution is obtained by integrating Cauchy’s equations, specialized in the absence of body forces and under the hypothesis of cylindrical bending

$$\tau_{13}^a(x_1, x_3; t) = - \int_h \sigma_{11,1}^{a(k)}(x_1, x_3; t) dx_3 \tag{8}$$

The axial stress $\sigma_{11}^{a(k)}$ that appears in Eq. (8) comes from the constitutive relation Eq. (5), with the strain quantities, i.e. the derivatives of the kinematic variables (see Eq. (4)) assumed to be new independent variables. According to this assumption, the axial

strain is rewritten as follows:

$$\varepsilon_{11}^{a(k)}(\mathbf{x}_1, \mathbf{x}_3; t) = e(\mathbf{x}_1; t) + \mathbf{x}_3 k(\mathbf{x}_1; t) + \mu^{(k)}(\mathbf{x}_3) k^\psi(\mathbf{x}_1; t) \quad (9)$$

where, $e(\mathbf{x}_1; t)$, $k(\mathbf{x}_1; t)$ and $k^\psi(\mathbf{x}_1; t)$ are the new strain variables. Using the mixed-form of the material constitutive relation, i.e. Eq. (5), to express the axial stress distribution in Eq. (8), $\sigma_{11.1}^{a(k)}$ is also depending on the assumed transverse normal stress, i.e. σ_{33}^a . This last term can be further manipulated in order to condense the additional stress variables and reduce the total number of unknowns. An intermediate step given by the mixed variational statement is required prior to performing the integration of Cauchy's equation, Eq. (8), to obtain the final expression of the assumed transverse shear stress distribution.

2.3. Mixed-variational statement and equations of motion

In order to reduce the number of unknown variables, to obtain the governing equations, and to develop a suitable FE formulation of the mixed-beam model $\text{RZT}_{\{3,2\}}^{(m)}$, a mixed-variational principle is required since more independent fields are present in the $\text{RZT}_{\{3,2\}}^{(m)}$ model: the displacement field (Eq. (1)) and the transverse stress field (Eqs. (6) and (8)). Among the existing mixed-variational statements, the Hellinger-Reissner (HR) functional [47] can be adopted. According to its definition (see Ref. [47]), the HR functional allows displacements and stresses to vary independently while still ensuring the strain compatibility between the quantities derived from the displacement and stress fields. This condition, enforced in integral (or weak) form, improves the predictive accuracy of both displacements and stress quantities, especially in FE formulation, as shown in Refs. [50,51].

The dynamic version of the mixed-variational statement reads as follows:

$$\delta\Pi = \delta\Pi_{\text{int}} + \delta\Pi_{\text{HR}} + \delta\Lambda - \delta\Pi_{\text{in}} = 0 \quad (10)$$

where δ denotes the virtual variation operator. The contributions that appear in Eq. (10) are defined as

$$\delta\Pi_{\text{int}} = \int_V [(\delta\varepsilon_{11}^{(k)} \sigma_{11}^{(k)} + \delta\gamma_{13}^{(k)} \tau_{13}^a + \delta\varepsilon_{33} \sigma_{33}^a)] dV \quad (11)$$

is the virtual variation of the internal energy;

$$\delta\Pi_{\text{in}} = - \int_V \rho^{(k)} \left(\delta U_1^{(k)} \ddot{U}_1^{(k)} + \delta U_3 \ddot{U}_3 \right) dV \quad (12)$$

is the virtual work of the inertia forces (where overdot indicates the differentiation with respect to time);

$$\delta\Pi_{\text{HR}} = \int_V [\delta\tau_{13}^a (\gamma_{13}^{(k)} - \gamma_{13}^{(k)a}) + \delta\sigma_{33}^a (\varepsilon_{33} - \varepsilon_{33}^{(k)a})] dV \quad (13)$$

is the Hellinger-Reissner variational contribution, which enforces in a weak manner the compatibility conditions between the transverse shear and normal strains coming from the assumed stress field with those derived from the displacement field.

From a mathematical point of view, the assumed stress quantities in Eq. (13) play the role of a Lagrangian multiplier in the compatibility conditions, ensuring that the strains derived from the displacement field are consistent with the deformation state as originated by the assumed stress field.

The penalty functional introduced in Eq. (10) and expressed by the symbol $\delta\Lambda$, enforces in a weak manner the compatibility conditions between the set of new strain variables and the quantities coming from the displacement-strain relations, see Eq. (9). The introduced penalty parameter, i.e. η (in this formulation $\eta = 10^{-3}$), controls the relative importance of the penalty condition in the overall governing functional. Its expression, according to the $\text{RZT}_{\{3,2\}}^{(m)}$ model, reads:

$$\delta\Lambda = \frac{1}{\eta} \int_V [(\delta u_{,1} - \delta e)(u_{,1} - e) + (\delta\theta_{,1} - \delta k)(\theta_{,1} - k) + (\delta\psi_{,1} - \delta k^\psi)(\psi_{,1} - k^\psi)] dV \quad (14)$$

In order to condense out the transverse normal stress variables, i.e. σ_2^z and σ_3^z , the first step of the beam model formulation is to enforce the transverse normal strain compatibility in the Hellinger-Reissner functional. This condition reads:

$$\int_V \delta\sigma_{33}^a (\varepsilon_{33} - \varepsilon_{33}^{(k)a}) dV = 0 \quad (15)$$

where, using Eq. (5),

$$\varepsilon_{33}^{(k)a}(\mathbf{x}_1, \mathbf{x}_3) = S_{33}^{(k)} \sigma_{33}^a(\mathbf{x}_1, \mathbf{x}_3) - \nu_{13}^{(k)} \varepsilon_{11}^{(k)}(\mathbf{x}_1, \mathbf{x}_3) \quad (16)$$

After substituting Eq. (16) into Eq. (15), a relationship is obtained between the transverse normal stress variables and the kinematic

ones, thus leading to the following expression:

$$\sigma_{33}^a(x_1, x_3; t) = A_\sigma^u(x_3)u_{,1}(x_1; t) + A_\sigma^\theta(x_3)\theta_{,1}(x_1; t) + A_\sigma^\psi(x_3)\psi_{,1}(x_1; t) + \mathbf{A}_\sigma^w(x_3)\mathbf{w}(x_1; t) \quad (17)$$

where $\mathbf{w}^T = [w^{(0)} \quad w^{(1)} \quad w^{(2)}]$. The through-the-thickness functions of the transverse coordinate that appear in Eq. (17) are reported for the sake of conciseness in Appendix A.

Substituting Eq. (17) into the constitutive relations, i.e., Eq. (5), and adopting the new strain variables, i.e., Eq. (9), the new expression of the axial stress reads:

$$\begin{aligned} \sigma_{11}^{a(k)}(x_1; t) = & (E_1^{(k)} + \nu_{13}^{(k)}A_\sigma^u(x_3))e(x_1; t) + (x_3E_1^{(k)} + \nu_{13}^{(k)}A_\sigma^\theta(x_3))k(x_1; t) + \\ & + (E_1^{(k)}\mu^{(k)}(x_3) + \nu_{13}^{(k)}A_\sigma^\psi(x_3))k^\psi(x_1; t) + \nu_{13}^{(k)}\mathbf{A}_\sigma^w(x_3)\mathbf{w}(x_1; t) \end{aligned} \quad (18)$$

Substituting Eq. (18) into Eq. (8), integrating along the thickness direction and enforcing the equilibrium with the prescribed tractions we obtain:

$$\tau_{13}^a(x_1, x_3; t) = \widehat{A}^z(x_3)e_{,1}(x_1; t) + \widehat{B}^z(x_3)k_{,1}(x_1; t) + \widehat{D}^z(x_3)k_{,1}^\psi(x_1; t) + \widehat{E}^z(x_3)\partial\mathbf{w}(x_1; t) = \mathbf{Z}_t(x_3)\mathbf{q}_t(x_1; t) \quad (19)$$

where $\mathbf{q}_t(x_1; t)^T = [e_{,1}(x_1; t) \quad k_{,1}(x_1; t) \quad k_{,1}^\psi(x_1; t) \quad \partial\mathbf{w}(x_1; t)^T]$ is the vector of the derivatives of the strain unknowns and transverse displacement variables. Moreover, $\partial\mathbf{w}(x_1; t)^T = [w_{,1}^{(0)} \quad w_{,1}^{(1)} \quad w_{,1}^{(2)}]$.

By substituting the expression of the displacement field, Eq. (1), into the strain-displacements relations and taking into account the mixed material constitutive equations, Eq. (5), the assumed transverse normal stress, Eq. (17), and transverse shear stress, Eq. (19), into the variational statement, Eq. (10), and integrating by parts, the equations of motion of the RZT_{3,2}^(m) model are obtained:

$$\begin{aligned} \delta u : N_{,1} + \frac{1}{\eta}(u_{,11} - e_{,1}) &= m^{(0)}\ddot{u} + m^{(1)}\dot{\theta} + m_\mu^{(0)}\ddot{\psi} \\ \delta w^{(0)} : Q_1^{w0} - N_1^z - \widehat{Q}^{w0} &= m^{(0)}\ddot{w}^{(0)} + m^{(1)}\dot{w}^{(1)} + m^{(2)}\ddot{w}^{(2)} \\ \delta w^{(1)} : Q_1^{w1} - N_2^z - \widehat{Q}^{w1} &= m^{(1)}\ddot{w}^{(0)} + m^{(2)}\dot{w}^{(1)} + m^{(3)}\ddot{w}^{(2)} \\ \delta w^{(2)} : Q_1^{w2} - N_3^z - \widehat{Q}^{w2} &= m^{(2)}\ddot{w}^{(0)} + m^{(3)}\dot{w}^{(1)} + m^{(4)}\ddot{w}^{(2)} \\ \delta \theta : M_{,1} - Q + \frac{1}{\eta}(\theta_{,11} - k_{,1}) &= m^{(1)}\ddot{u} + m^{(2)}\dot{\theta} + m_\mu^{(1)}\ddot{\psi} \\ \delta \psi : M_{,1}^\psi - Q^\psi + \frac{1}{\eta}(\psi_{,11} - k_{,1}^\psi) &= m_\mu^{(0)}\ddot{u} + m_\mu^{(1)}\dot{\theta} + m_\mu^{(2)}\ddot{\psi} \\ \delta e : -\frac{1}{\eta}(e - u_{,1}) + E^{HR} &= 0 \\ \delta k : -\frac{1}{\eta}(k - \theta_{,1}) + K^{HR} &= 0 \\ \delta k^\psi : -\frac{1}{\eta}(k^\psi - \psi_{,1}) + K_\psi^{HR} &= 0 \end{aligned} \quad (20)$$

along with the consistent boundary conditions:

$$\begin{aligned} u = \bar{u} \quad \text{on } x_1 = 0, L \vee \bar{N} + \frac{1}{\eta}(u_{,1} - e) \quad \text{on } x_1 = 0, L \\ w^{(0)} = \bar{w}^{(0)} \quad \text{on } x_1 = 0, L \vee \bar{Q}^{w0} + {}^{HR}\bar{Q}_1^{w0} \quad \text{on } x_1 = 0, L \\ w^{(1)} = \bar{w}^{(1)} \quad \text{on } x_1 = 0, L \vee \bar{Q}^{w1} + {}^{HR}\bar{Q}_1^{w1} \quad \text{on } x_1 = 0, L \\ w^{(2)} = \bar{w}^{(2)} \quad \text{on } x_1 = 0, L \vee \bar{Q}^{w2} + {}^{HR}\bar{Q}_1^{w2} \quad \text{on } x_1 = 0, L \\ \theta = \bar{\theta} \quad \text{on } x_1 = 0, L \vee \bar{M} + \frac{1}{\eta}(\theta_{,1} - k_{11}) \quad \text{on } x_1 = 0, L \\ \psi = \bar{\psi} \quad \text{on } x_1 = 0, L \vee \bar{M}^\psi + \frac{1}{\eta}(\psi_{,1} - k^\psi) \quad \text{on } x_1 = 0, L \\ e = \bar{e} \quad \text{on } x_1 = 0, L \vee {}^{HR}\bar{E}_1^e \quad \text{on } x_1 = 0, L \\ k = \bar{k} \quad \text{on } x_1 = 0, L \vee {}^{HR}\bar{K}_1^k \quad \text{on } x_1 = 0, L \\ k^\psi = \bar{k}^\psi \quad \text{on } x_1 = 0, L \vee {}^{HR}\bar{K}_1^{k^\psi} \quad \text{on } x_1 = 0, L \end{aligned} \quad (21)$$

where the resultant forces, moments, and inertia coefficients are defined as follows:

$$\begin{aligned}
 (N, M, M^\phi) &= \langle (1, x_3, \mu^{(k)}(x_3)) \sigma_{11}^{(k)} \rangle; \\
 N^z &= \langle \mathbf{H}_3^z T \sigma_{33}^a \rangle; \\
 (Q^w, Q, Q^\phi) &= \langle (\mathbf{H}^z T, 1, \mu^{(k)}) \tau_{13}^a \rangle
 \end{aligned}
 \tag{22}$$

$$\begin{aligned}
 (m^{(0)}, m^{(1)}, m^{(2)}, m^{(3)}, m^{(4)}) &= \langle \rho^{(k)}(1, x_3, x_3^2, x_3^3, x_3^4) \rangle; \\
 (m_\mu^{(0)}, m_\mu^{(1)}, m_\mu^{(2)}) &= \langle \rho^{(k)}(\mu^{(k)}, x_3 \mu^{(k)}, (\mu^{(k)})^2) \rangle
 \end{aligned}
 \tag{23}$$

Moreover, $\mathbf{H}^z = [1 \quad x_3 \quad x_3^2]$.

By using Eqs. (5), (17) and (19), the RZT_{3,2}^(m) beam constitutive relations are obtained as follows:

$$\begin{aligned}
 N &= \tilde{A} u_{,1} + \tilde{B} \theta_{,1} + \tilde{A}^\phi \psi_{,1} + \tilde{A}^w \mathbf{w} \\
 M &= \tilde{C} u_{,1} + \tilde{D} \theta_{,1} + \tilde{B}^\phi \psi_{,1} + \tilde{B}^w \mathbf{w} \\
 M^\phi &= \tilde{E}^\phi u_{,1} + \tilde{F}^\phi \theta_{,1} + \tilde{G}^\phi \psi_{,1} + \tilde{C}^w \mathbf{w}
 \end{aligned}
 \tag{24}$$

$$\mathbf{N}^z = \mathbf{A}^{Nz} u_{,1} + \mathbf{B}^{Nz} \theta_{,1} + \mathbf{C}^{Nz} \psi_{,1} + \mathbf{D}^{Nz} \mathbf{w}
 \tag{25}$$

$$\begin{aligned}
 Q^w &= \hat{\mathbf{A}}^{wT} e_{,1} + \hat{\mathbf{B}}^{wT} k_{,1} + \hat{\mathbf{C}}^{wT} k_{,1}^\psi + \hat{\mathbf{D}}^{wT} \partial \mathbf{w} \\
 Q &= \hat{\mathbf{A}}^\theta e_{,1} + \hat{\mathbf{B}}^\theta k_{,1} + \hat{\mathbf{C}}^\theta k_{,1}^\psi + \hat{\mathbf{D}}^{\theta T} \partial \mathbf{w} \\
 Q^\phi &= \hat{\mathbf{A}}^\psi e_{,1} + \hat{\mathbf{B}}^\psi k_{,1} + \hat{\mathbf{C}}^\psi k_{,1}^\psi + \hat{\mathbf{D}}^{wT} \partial \mathbf{w}
 \end{aligned}
 \tag{26}$$

For the sake of clarity, the other quantities that appear in the governing equations, boundary conditions, and constitutive relations are reported in [Appendix A](#).

3. Finite element formulation

This section summarizes the formulation of a simple two-node beam element based on the RZT_{3,2}^(m) for the free-vibration analysis of thick sandwich beams.

In the expressions of the mixed variational statement, see Eqs. (11)–(14), the order of differentiation with respect to the axial coordinate does not exceed the first. Thus, the shape functions that can approximate the distribution of the unknown variables must satisfy only C⁰ – continuity requirement.

As a direct consequence, a finite element based on this kind might be affected by shear-locking issues when used for slender beams. However, since this work focuses on the study of thick sandwich beams, the influence of shear-locking is not relevant, and the well-known strategies commonly adopted to mitigate its effect are not addressed here.

Furthermore, from a mathematical point of view, the mixed-finite element formulation leads to a typical saddle-point problem governed by complex mathematical relations that must be satisfied, as detailed by Babuska [53] and Brezzi [54]. These requirements, also known as the Babuska-Brezzi condition, limit the selection range of possible shape functions in the mixed-element formulation in order to avoid stability issues and inconsistencies of the final numerical results.

From a practical point of view, and in order to ensure the problem solvability, the Babuska-Brezzi condition can be stated as follows: the number of degrees of freedom (dofs) used to approximate the kinematic unknowns must be equal to or greater than those used to approximate the stress field.

3.1. Interpolation scheme

In virtue of the previous considerations, the simplest and lowest-order beam element is the isoparametric one, which is formulated by approximating each unknown variable using the linear Lagrangian polynomials. For clarity, let us group the kinematic and the strain unknown variables into two different vectors, i.e. $\mathbf{d}_d^T = [u \ w^{(0)} \ w^{(1)} \ w^{(2)} \ \theta \ \psi]$ and $\mathbf{d}_s^T = [e \ k \ k^\psi]$, as follows:

$$\begin{Bmatrix} \mathbf{d}_d(x_1; t) \\ \mathbf{d}_s(x_1; t) \end{Bmatrix} = \begin{bmatrix} \mathbf{N}_d(x_1) & \mathbf{0} \\ \mathbf{0} & \mathbf{N}_s(x_1) \end{bmatrix} \begin{Bmatrix} \mathbf{q}_d^{(e)}(t) \\ \mathbf{q}_s^{(e)}(t) \end{Bmatrix}
 \tag{27}$$

where the shape function matrices, e.g. $\mathbf{N}_d(x_1)$ and $\mathbf{N}_s(x_1)$ that appear in Eq. (27), read

$$\mathbf{N}_d = \begin{bmatrix} \mathbf{L} & \mathbf{0} & \mathbf{0} & \mathbf{0} \\ & \mathbf{L}^w & \mathbf{0} & \mathbf{0} \\ & & \mathbf{L} & \mathbf{0} \\ sym. & & & \mathbf{L} \end{bmatrix}; \quad \mathbf{N}_s = \begin{bmatrix} \mathbf{L} & \mathbf{0} & \mathbf{0} \\ & \mathbf{L} & \mathbf{0} \\ sym. & & \mathbf{L} \end{bmatrix}; \quad \mathbf{L}^w = \begin{bmatrix} \mathbf{L} & \mathbf{0} & \mathbf{0} \\ & \mathbf{L} & \mathbf{0} \\ sym. & & \mathbf{L} \end{bmatrix}
 \tag{28}$$

Moreover, in Eq. (27), the vectors of the elemental nodal degrees of freedom read:

$$\mathbf{q}_d^{(e)T} = \left[\mathbf{q}^{uT} \quad \mathbf{q}^{wT} \quad \mathbf{q}^{\theta T} \quad \mathbf{q}^{\psi T} \right]; \quad \mathbf{q}_s^{(e)T} = \left[\mathbf{q}^{eT} \quad \mathbf{q}^{kT} \quad \mathbf{q}^{k\psi T} \right] \quad (29)$$

and, for each sub-vector, we can write:

$$\mathbf{q}^{uT} = \left[u_1 \quad u_2 \right]; \quad \mathbf{q}^{wT} = \left[w_1^{(0)} \quad w_2^{(0)} \quad w_1^{(1)} \quad w_2^{(1)} \quad w_1^{(2)} \quad w_2^{(2)} \right]; \quad \mathbf{q}^{\theta T} = \left[\theta_1 \quad \theta_2 \right]; \quad \mathbf{q}^{\psi T} = \left[\psi_1 \quad \psi_2 \right] \quad (30)$$

$$\mathbf{q}^{eT} = \left[e_1 \quad e_2 \right]; \quad \mathbf{q}^{kT} = \left[k_1 \quad k_2 \right]; \quad \mathbf{q}^{k\psi T} = \left[k_1^\psi \quad k_2^\psi \right] \quad (31)$$

As anticipated, in Eq. (28) the elemental shape functions matrices are constituted by the Lagrangian shape functions defined in the natural coordinate system, i.e. $\xi = \left(2x_1/L^{(e)} - 1 \right) \in [-1, 1]$, where $L^{(e)}$ represents the beam element length. The vector of the linear shape functions is defined as follows,

$$\mathbf{L}(\xi) = \left[L_1(\xi) \quad L_2(\xi) \right] = \left[\frac{1}{2}(1 - \xi) \quad \frac{1}{2}(1 + \xi) \right] \quad (32)$$

3.2. Discrete equation of motion

The elemental stiffness and mass matrices of the 2-noded mixed-{3,2}-RZT beam element, here named with 2B – RZT_{3,2}^(m), are obtained by adopting the finite element approximation, i.e. Eq. (27), into the mixed variational statement given by Eq. (10). According to this procedure, the linear strain-displacement relations, Eq. (4), for an e th element read as follows:

$$\varepsilon_{11}^{(k)(e)} = \left[\mathbf{L}_1 \quad x_3 \mathbf{L}_1 \quad \mu^{(k)} \mathbf{L}_1 \right] \left\{ \begin{matrix} \mathbf{q}^u \\ \mathbf{q}^\theta \\ \mathbf{q}^\psi \end{matrix} \right\}^{(e)}; \quad \gamma_{13}^{(e)} = \left[\mathbf{H}^2 \mathbf{L}_1^w \quad \mathbf{L} \quad \mu_{,3}^{(k)} \mathbf{L} \right] \left\{ \begin{matrix} \mathbf{q}^w \\ \mathbf{q}^\theta \\ \mathbf{q}^\psi \end{matrix} \right\}^{(e)}; \quad \varepsilon_{33}^{(e)} = \mathbf{H}_{,3}^2 \mathbf{L}^w \mathbf{q}^{w(e)} \quad (33)$$

whereas the elemental assumed transverse normal and shear stresses, i.e. Eqs. (17) and (19), follow

$$\sigma_{33}^a{}^{(e)} = \left[\mathbf{A}_o^u \mathbf{L}_1 \quad \mathbf{A}_o^w \mathbf{L}^w \quad \mathbf{A}_o^\theta \mathbf{L}_1 \quad \mathbf{A}_o^\psi \mathbf{L}_1 \right] \mathbf{q}_d^{(e)} \quad (34)$$

$$\tau_{13}^a{}^{(e)} = \left[\widehat{\mathbf{E}}^z \mathbf{L}_1^w \quad \widehat{\mathbf{A}}^z \mathbf{L}_1 \quad \widehat{\mathbf{B}}^z \mathbf{L}_1 \quad \widehat{\mathbf{D}}^z \mathbf{L}_1 \right] \left\{ \begin{matrix} \mathbf{q}^w \\ \mathbf{q}_s \end{matrix} \right\}^{(e)} \quad (35)$$

The elemental assumed transverse shear strain in the Hellinger-Reissner term of the variational statement (see Eq. (13)) can be related to Eq. (35) with the material constitutive relation Eq. (5). Similarly, the elemental axial stress is obtained by substituting the elemental axial strain of Eq. (33) and the transverse normal stress, i.e., Eq. (34) into Eq. (5).

By proceeding with the appropriate substitutions and adopting the notation introduced by Eq. (27) to highlight the terms of the two groups of unknown variables, the discretized equations of motion for the free-vibration problem are expressed as follows:

$$\mathbf{M}^{(e)} \ddot{\mathbf{q}}^{(e)} + \mathbf{K}^{(e)} \mathbf{q}^{(e)} = \begin{bmatrix} \mathbf{M}_{dd}^{(e)} & \mathbf{0} \\ \mathbf{0}^T & \mathbf{0} \end{bmatrix} \left\{ \begin{matrix} \mathbf{q}_d^{(e)} \\ \mathbf{q}_s^{(e)} \end{matrix} \right\} + \begin{bmatrix} \mathbf{K}_{dd}^{(e)} & \mathbf{K}_{ds}^{(e)} \\ \mathbf{K}_{ds}^{(e)T} & \mathbf{K}_{ss}^{(e)} \end{bmatrix} \left\{ \begin{matrix} \mathbf{q}_d^{(e)} \\ \mathbf{q}_s^{(e)} \end{matrix} \right\} = \mathbf{0} \quad (36)$$

where the full expressions of the matrices in Eq. (36) are reported for clarity in Appendix B. In this work, no strategies to mitigate the shear locking problem are implemented, given that the numerical model is designed to study thick structures, full integration of stiffness and mass matrices requires only two-point Gauss quadrature.

According to the formulation, this element involves eighteen degrees of freedom (nine dofs for each node), which could be computationally expensive. Therefore, it is possible to adopt the static condensation technique to reduce the computational cost while maintaining the same numerical accuracy. The second line of Eq. (36) could be solved statically by making $\mathbf{q}_s^{(e)}$ depending on the $\mathbf{q}_d^{(e)}$ variables. It reads:

$$\mathbf{K}_{ds}^{(e)T} \mathbf{q}_d^{(e)} + \mathbf{K}_{ss}^{(e)} \mathbf{q}_s^{(e)} = \mathbf{0} \rightarrow \mathbf{q}_s^{(e)} = -\mathbf{K}_{ss}^{(e)-1} \mathbf{K}_{ds}^{(e)T} \mathbf{q}_d^{(e)} \quad (37)$$

Substituting Eq. (37) into Eq. (36), it yields a new expression of the equations of motion:

$$\mathbf{M}_{dd}^{(e)} \ddot{\mathbf{q}}_d^{(e)} + \left(\mathbf{K}_{dd}^{(e)} - \mathbf{K}_{ds}^{(e)} \mathbf{K}_{ss}^{(e)-1} \mathbf{K}_{ds}^{(e)T} \right) \mathbf{q}_d^{(e)} = \mathbf{0} \quad (38)$$

Finally,

$$\mathbf{M}_{dd}^{(e)} \mathbf{q}_d^{(e)} + \widehat{\mathbf{K}}_{dd}^{(e)} \mathbf{q}_d^{(e)} = \mathbf{0} \tag{39}$$

with $\widehat{\mathbf{K}}_{dd}^{(e)} = \left(\mathbf{K}_{dd}^{(e)} - \mathbf{K}_{ds}^{(e)} \mathbf{K}_{ss}^{(e)-1} \mathbf{K}_{ds}^{(e)T} \right)$.

It is worth noting that the strain-related degrees of freedom introduced in the mixed-model formulation do not add any inertia terms into the elemental mass matrix. Therefore, the static condensation described by Eqs. (37) and (38) does not introduce any approximation, even when solving a dynamic problem. This procedure reduces the overall number of elemental dofs from eighteen to twelve. Thus, the final topology of 2B – RZT_{3,2}^(m) element is displayed in Fig. 2.

For the sake of clarity, the formulation of the 2B – RZT_{3,2}^(m) element for dynamic analysis is summarized in the flowchart shown in Fig. 3.

4. Numerical assessment and element convergence analysis

In this section, a numerical assessment to evaluate the accuracy of the presented model, both analytical and FE one, is reported. The addressed problem is the dynamic free-vibrational behaviour of a multilayered symmetric cross-ply sandwich beam. The static analysis has already been presented, and the interested reader can refer to Ref. [50] for a comprehensive static response analysis assessment of the proposed model. The sandwich beam considered in this study, here referred as D0, has a length-to-thickness ratio $L/h = 4$, and a width, $b = 1$. Tables 1 and 2 report, respectively, the material characteristics and the laminate stacking sequence of the sandwich beam D0.

The sandwich beam is simply supported on both edges, and, according to the analytical RZT_{3,2}^(m) model, the boundary conditions are

$$\begin{aligned} \textcircled{0}x_1 = 0, L \\ \mathbf{w}^{(0)} = \mathbf{w}^{(1)} = \mathbf{w}^{(2)} = e = k = k^\psi = 0 \\ N + \frac{1}{\eta} (u_{,1} - e) = M + \frac{1}{\eta} (\theta_{,1} - k) = M^\psi + \frac{1}{\eta} (\psi_{,1} - k^\psi) = 0 \end{aligned} \tag{40}$$

For this beam configuration, the exact Navier analytical solution of the RZT_{3,2}^(m) model able to satisfy both governing equations and boundary conditions, is based on the following trigonometric expressions:

$$\begin{aligned} u_1(x_1; t) &= \sum_{m=1}^M U_m \cos(\lambda_m x_1) \sin(\omega_m t); \\ \mathbf{w}^{(0)}(x_1; t) &= \sum_{m=1}^M \mathbf{W}_m^{(0)} \sin(\lambda_m x_1) \sin(\omega_m t); \\ \mathbf{w}^{(1)}(x_1; t) &= \sum_{m=1}^M \mathbf{W}_m^{(1)} \sin(\lambda_m x_1) \sin(\omega_m t); \\ \mathbf{w}^{(2)}(x_1; t) &= \sum_{m=1}^M \mathbf{W}_m^{(2)} \sin(\lambda_m x_1) \sin(\omega_m t); \\ \theta(x_1; t) &= \sum_{m=1}^M \Theta_m \cos(\lambda_m x_1) \sin(\omega_m t); \\ \psi(x_1; t) &= \sum_{m=1}^M \Psi_m \cos(\lambda_m x_1) \sin(\omega_m t); \\ e(x_1; t) &= \sum_{m=1}^M E_m \sin(\lambda_m x_1) \sin(\omega_m t); \\ k(x_1; t) &= \sum_{m=1}^M K_m \sin(\lambda_m x_1) \sin(\omega_m t); \\ k^\psi(x_1; t) &= \sum_{m=1}^M K_m^\psi \sin(\lambda_m x_1) \sin(\omega_m t); \end{aligned} \tag{41}$$

where $\lambda_m = m\pi/L$ is the half-wave number in x_1 direction, and ω_m is the m th circular frequency.

If not otherwise specified, the following normalized frequency is considered

$$\bar{f}_m = \frac{\omega_m L^2}{2\pi} \sqrt{\frac{\rho^{(1)}}{E_2^{(1)}}} \tag{42}$$

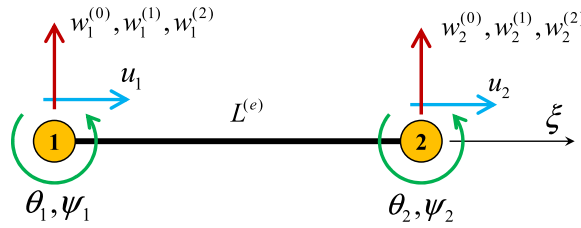


Fig. 2. Final topology of 2B – RZT_{3,2}^(m) element.

For comparison purposes, a reference solution for the first 6 fundamental frequencies corresponding to the flexural modes has been obtained using a high-fidelity FE model developed with the MSC-NASTRAN commercial software [55]. Taking advantage of the cylindrical bending assumptions, the D0 beam has been modelled in the (x₁, x₃) plane using 40000 membrane QUAD8 MSC-NASTRAN elements, i.e. 242002 dofs.

In Table 3, a comparison is presented between the first six normalized flexural circular frequencies obtained analytically with RZT_{3,2}^(m) and the reference ones obtained with MSC-NASTRAN. It is worth noting that the mixed-RZT model accurately predicts the first six frequencies with an error less than 0.3 % in absolute value, for the first four fundamental frequencies. The errors in frequency estimation for the 5th and 6th modes seem slightly higher than those obtained for the lower modes.

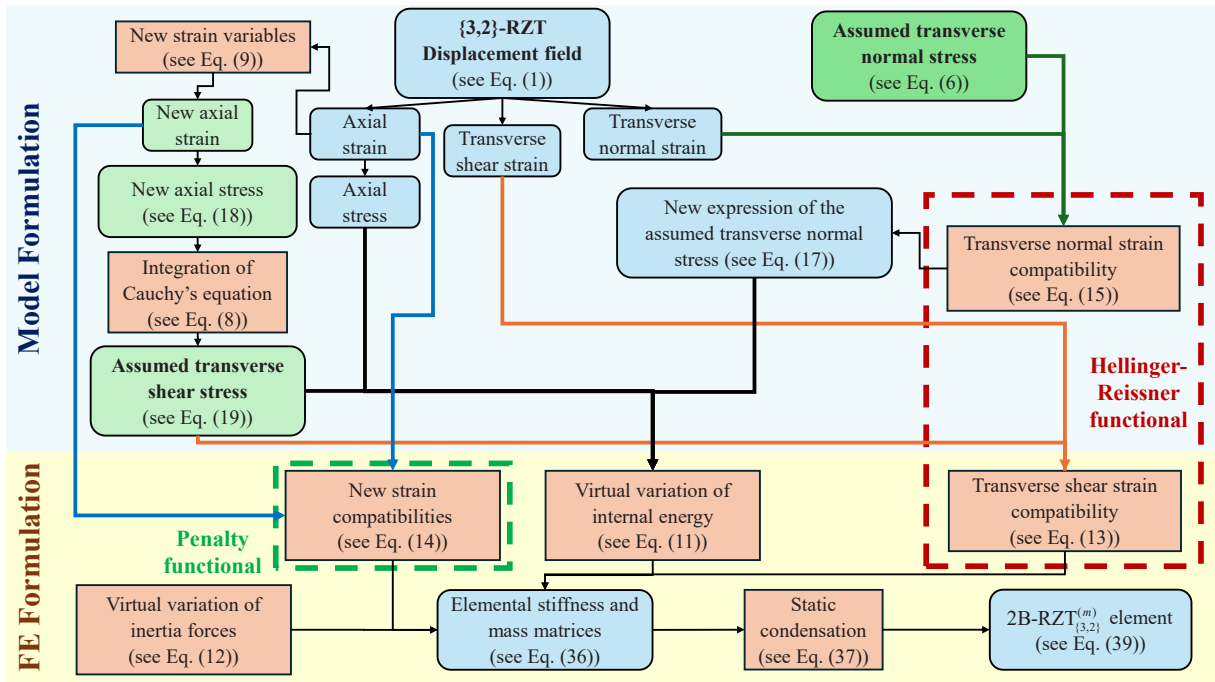


Fig. 3. Flowchart of the 2B – RZT_{3,2}^(m) element formulation for free-vibration problems.

Table 1
Material nomenclature and properties. The elastic moduli are in MPa, and the density in kg/m³.

Material Name	E ₁	E ₂	E ₃	ν ₁₂	ν ₁₃	ν ₂₃	G ₁₂	G ₁₃	G ₂₃	ρ
A	110000	7857	7857	0.33	0.33	0.49	3292	3292	1292	1600
B	40.3	40.3	40.3	0.3	0.3	0.3	12	12	12	112

Table 2
Laminate stacking sequences and nomenclature. The orientations are given in degrees.

Laminate ID	Normalized thickness h ^(k) /h	Lamina materials	Lamina orientations [°]
D0	0.05/0.05/0.8/0.05/0.05	A/A/B/A/A	0/90/Core/90/0

This discrepancy can be better understood by examining the through-the-thickness distribution of the axial displacement on the left supported end corresponding to the 4th, 5th and 6th modes (Fig. 4).

Although a third-order zigzag function is included in the proposed $RZT_{\{3,2\}}^{(m)}$ model, for this particular sandwich configuration characterized by a soft core with low transverse shear modulus, it is not fully able to reproduce an accurate through-the-thickness variation of the axial displacement in the core layer. In fact, in such a laminate configuration, the ω_0, χ_0 quantities assume very low values and the parabolic and cubic terms are almost null. Additionally, the through-the-thickness distribution of the third-order zigzag function in Eq. (2) is fixed once the lamination scheme is chosen, since it is related to the laminate thickness and transverse shear material properties. Consequently, the third-order zigzag function $\mu^{(k)}(x_3)$ is invariant with respect to the modal shape considered. According to these considerations, for the 4th normal mode, the differences in the through-the-thickness distribution between $RZT_{\{3,2\}}^{(m)}$ and MSC-NASTRAN are limited as the non-linear behaviour is not particularly pronounced. However, for modes 5 and 6, the differences become more significant as, in these cases, the complex distribution of the axial displacement within the core is not reproduced correctly by the zigzag function in the $RZT_{\{3,2\}}^{(m)}$ model, resulting in a larger errors in both mass and stiffness estimation related to the zigzag effect, and therefore in the corresponding natural frequencies, as reported in Table 3. Nevertheless, despite these limitations in the core layer for soft materials, the accuracy across the face-sheets' thickness remains quite remarkable.

The reference analytical results of $RZT_{\{3,2\}}^{(m)}$ reported in Table 3 are also used to evaluate the convergence behaviour of the corresponding 2B- $RZT_{\{3,2\}}^{(m)}$ elements. Fig. 5 reports the convergence curves, in terms of the ratio between the FEM value and the analytical one (reported in Table 3), for the first three modes. The number of elements considered in this convergence study is: 16, 32, 64, 128, 256, 512, 1024, 2048, and 4096. The convergence to the analytical solution is very fast, especially for the fundamental frequency.

These results demonstrate the computational advantage of the 2B- $RZT_{\{3,2\}}^{(m)}$ elements in computing accurate frequencies at a lower computational cost with respect to the high-fidelity FE models.

5. Experimental assessment

This section describes the experimental campaign conducted to assess the performance and predictive capabilities of the formulated mixed- $\{3,2\}$ RZT beam element for the dynamic free-vibration analysis of thick sandwich beams. The experimental activity has been conducted at the LAQ-AERMEC laboratory of the Mechanical and Aerospace Engineering Department (DIMEAS) of the Politecnico di Torino. The sandwich beam specimens have been manufactured by the Department of Science and Aerospace Technology of Politecnico di Milano.

5.1. Beam specimens

The sandwich beams (shown in Fig. 6) are made of two aluminium alloy (EN-AW7075-T6) face-sheets, bonded together with a thick Rohacell® WF110 polymethacrylamide foam core. In each beam specimen, the core layer is bonded with the face-sheets with a 0.25 mm 3M® Scotch-Weld® Structural Adhesive Film AF 163-2K.

In order to investigate the effect of the length-to-thickness ratio, different thicknesses for the core and the face-sheets have been considered. Let us denote with h_f the thickness of each face-sheet and with h_c the thickness of the core layer (obtained as the difference between the total thickness h , the adhesive layer, and the aluminium alloy face-sheet thicknesses). All the beam specimens have a length-to-thickness ratio below 20, which is in the range from moderately thick to thick structures. Table 4 reports the nomenclature and beam dimensions.

Except for the adhesive layer, whose properties have been taken from the producer datasheet [56], the mechanical properties of the aluminium alloy and of the WF110 Rohacell® foam have been experimentally determined, and their results are reported in Table 5. The details of the characterization methodology can be found in Ref. [57].

Table 3

First six flexural normalized frequencies, i.e. \bar{f}_m , of $RZT_{\{3,2\}}^{(m)}$ for simply-supported sandwich DO beam ($L/h=4$). In brackets, the percent errors with respect to the reference MSC-NASTRAN solution.

Mode	MSC-NASTRAN	RZ $T_{\{3,2\}}^{(m)}$
1	177.02	176.93 (−0.05 %)
2	430.86	430.79 (−0.02 %)
3	796.19	796.80 (0.08 %)
4	1276.21	1272.79 (−0.27 %)
5	1852.95	1815.38 (−2.03 %)
6	2474.66	2304.25 (−6.89 %)

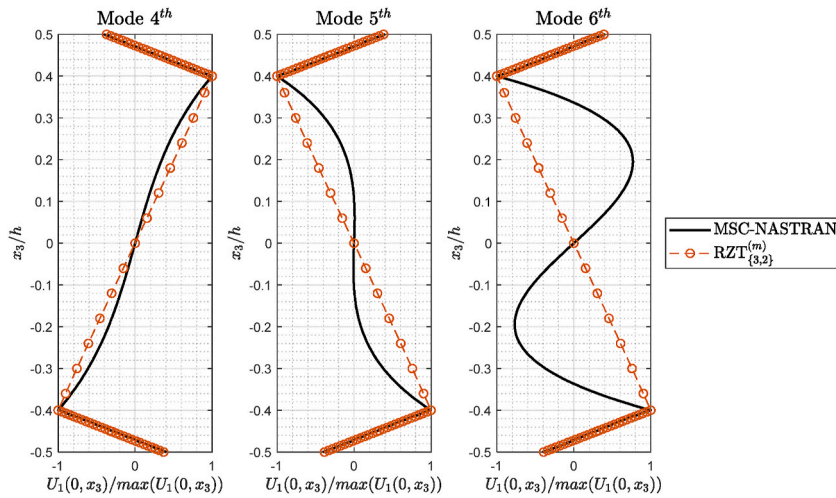


Fig. 4. Through-the-thickness distributions of the axial displacement on the left supported end corresponding to the 4th, 5th and 6th modes obtained with MSC-NASTRAN and with the $RZT_{\{3,2\}}^{(m)}$ solution. Results are normalized with respect to the maximum value of the through-the-thickness axial displacement distribution for each mode.

5.2. Experimental set-up and numerical models

The beam specimens D1, D2, D3, and D4 have been experimentally tested to evaluate their natural frequencies and the corresponding modal shapes for free-free boundary conditions. Prior to performing the experimental modal analysis and with the aim of estimating the frequency bandwidth of the first five flexural mode shapes, high-fidelity FE models of the four sandwich beams have been created using MSC-NASTRAN. In particular, both the aluminium alloy face-sheets and the WF110 foam core have been modelled using parabolic HEXA20 solid elements. For simplicity to mesh and in order to keep the amount of used elements contained, the adhesive layers have not been considered in the 3D models. Table 6 summarizes the number of elements adopted for each model and the computational cost in terms of the total number of degrees of freedom (dofs) for each sandwich beam specimen.

The Experimental Modal Analysis (EMA) has been performed using the LASER Doppler Vibrometer (LDV) methodology. A Polytec PSV-500 scanning LASER head and its frontend equipment have been used to measure the velocity responses of 69 scanned points over the whole beam, according to the scheme reported in Fig. 7a). All the points are located on the external top surface of the beam, i.e. $x_3 = +h/2$. The reference point 0, i.e. where the excitation force is applied, is on the bottom sandwich external surface, at the coordinates $x_1 = 350$ mm, $x_2 = -15$ mm, and $x_3 = -h/2$. The scheme has been obtained through the estimation of the numerical mode shapes provided by the high-fidelity MSC-NASTRAN FE models, see Table 6. Due to the reflective properties of the aluminium alloy, the quality of the LASER measurements in the scanned point has been increased using appropriate reflectors, as observable in Fig. 7b).

The excitation force has been applied at point 0, chosen as a reference point, using an electrodynamic shaker (K2007E01, up to 9

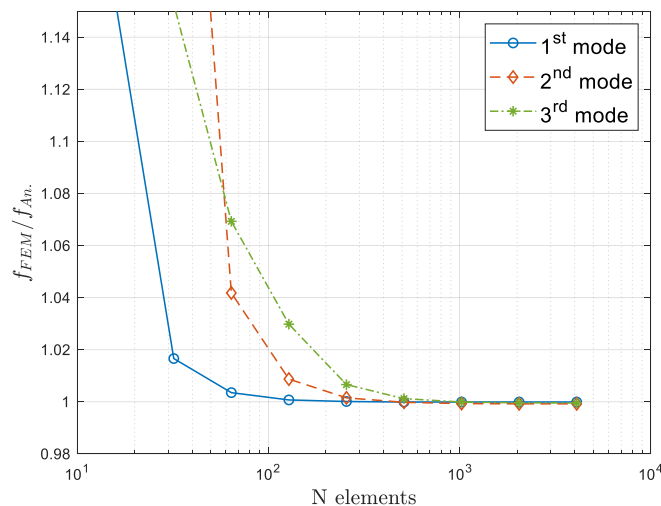


Fig. 5. Convergence results for the first three normal frequencies of simply supported beam D0, using the $2B-RZT_{\{3,2\}}^{(m)}$ elements.

kHz and up to 67 N of applied force) connected with a stinger to the sandwich beam specimens. The excitation force signal is a periodic chirp function of constant amplitude and varying in frequency from 400 Hz (since no frequencies were expected below this value) to 4 kHz. The amplitudes and the LASER sensitivities have been calibrated differently due to the different dynamic behaviour of the sandwich beam specimens. An impedance head (PCB Piezotronics, Inc. – model 288D01) has been glued on the beam at the excitation point (as shown in Fig. 8) to measure the force intensity and the corresponding response acceleration in order to perform the modal parameter estimation.

The sandwich specimens were hanged to the support system made of steel using cable ties and rubber bands to simulate the free-free boundary conditions, see Fig. 9. For each scanned point, an average of 40 Frequency Response Functions (FRFs) is obtained through the PSV software in order to increase the signal-to-noise ratio and improve the quality of the measurements. According to the scanned and reference points disposal, both flexural and torsional mode shapes have been experimentally observed and determined. However, only the results for the flexural modes have been considered in this assessment.

5.3. Experimental-numerical assessment

The experimental FRFs of the whole scanned points have been processed by LSM-Siemens Test.Lab. The PolyMAX algorithm, implemented in Test.Lab and based on the least square complex exponential algorithm, was used to estimate the modal parameters [58,59].

According to the previous convergence analysis, the sandwich beam specimens have been modelled with 4096 $2B - RZT_{\{3,2\}}^{(m)}$ elements, which corresponds to 24576 dofs. The analyses using the MSC-NASTRAN software on the 3D sandwich beam models presented in Table 6 were performed on a machine equipped with an Intel Core i7-10750H CPU (12 cores, 2.9 GHz base frequency), 16 GB of RAM, and running Windows 11. Table 7 presents the CPU times (in seconds) required for each sandwich beam analysis using both the MSC-NASTRAN software and the FE code developed in MATLAB®, which implements the $2B - RZT_{\{3,2\}}^{(m)}$ elements. All the MATLAB® simulations were carried out on the same machine. Due to the high computational cost, the MSC-NASTRAN simulations were performed only once per case, whereas for the MATLAB® code using the $2B - RZT_{\{3,2\}}^{(m)}$ elements, the reported CPU times in Table 7 correspond to the average of 10 runs for each sandwich configuration. Moreover, the speedup (defined as the ratio between the MSC-NASTRAN time and the MATLAB®- $2B - RZT_{\{3,2\}}^{(m)}$ one) is also presented in Table 7 to provide a quantitative evaluation of the computational efficiency.

From Tables 7 and it is worth noting that the average CPU times using the $2B - RZT_{\{3,2\}}^{(m)}$ model for each sandwich beam remain nearly constant, with only minor variations. This expected outcome is due to the fact that each beam model has the same number of elements, and the variation in the sandwich configuration does not influence the CPU time. This happens because one of the main advantages of the $2B - RZT_{\{3,2\}}^{(m)}$ formulation is that the zigzag functions and the integrals over the thickness can be performed in a simple manner during the pre-processing phase. Moreover, the speedup of the proposed model with respect to the reference 3D solution is remarkable, ranging from 33x to 41x, reducing the computational time by more than one order of magnitude.

In Table 8, Table 9, Tables 10 and 11, the experimental natural frequencies of the first four flexural modes, those computed with the $2B - RZT_{\{3,2\}}^{(m)}$ elements, and those obtained with the 3D MSC-NASTRAN models are reported. In addition, the corresponding experimental modal damping factors computed using the PolyMAX algorithm have been reported for each mode. Finally, the relative percent errors with respect to the experimental results are shown in brackets.

As shown in Tables 8–11, the $2B - RZT_{\{3,2\}}^{(m)}$ solution exhibits natural frequencies lower than the experimental ones, with errors

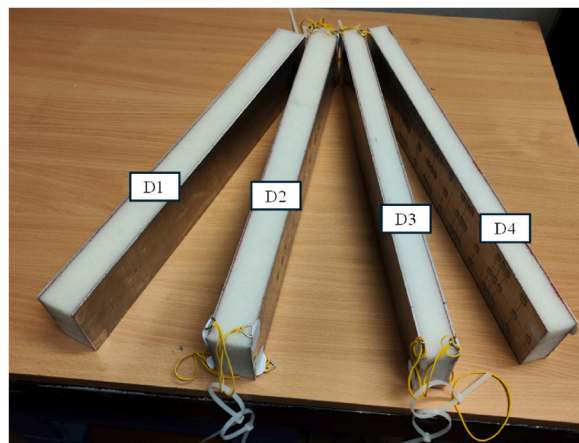


Fig. 6. Sandwich beam specimens.

Table 4
Sandwich beam specimens nomenclature and dimensions (in mm).

Specimen ID	L	b	h	h_f	h_c	L/h	h_c/h_f
D1	500.00	80.00	43.32	2.00	38.82	11.54	19.41
D2	500.00	80.00	41.18	1.00	38.68	12.14	38.68
D3	500.00	80.00	33.53	2.00	29.03	14.91	14.52
D4	500.00	80.00	31.54	1.00	29.04	15.85	29.04

Table 5
Materials' mechanical properties. Young's and shear moduli are in MPa, and density in kg/m^3 .

Material	E	G	ρ
EN-AW7075-T6	67545	25393	2751
Rohacell® WF110	194	67	110
3M® Scotch-Weld® AF 163-2K [56]	1110	414	121

ranging from -3.7% to -14.2% for some modal shapes. These differences cannot be explained in this case by the limitations of the model associated with the third-order zigzag function, since the core layer is stiff enough to limit the occurrence of complex patterns in the axial displacements to higher modes. Moreover, a similar behaviour in lower frequencies estimation is also observable in the MSC-NASTRAN results, which are different from those coming from $2B - RZT_{\{3,2\}}^{(m)}$ analysis by no more than 3% . This last consideration emphasizes not only the computational efficiency of the $2B - RZT_{\{3,2\}}^{(m)}$ elements, but also their accuracy in reproducing the results

Table 6
Number of elements and computational costs (in terms of total dofs) of MSC-NASTRAN 3D models, with details for the core and single face-sheet meshes, including the number of elements along the three directions.

Specimen ID	N. of Elements	Dofs
D1	210000 Core: 250x40x19 Single face-sheet: 250x40x1	679206
D2	210000 Core: 250x40x19 Single face-sheet: 250x40x1	679206
D3	170000 Core: 250x40x15 Single face-sheet: 250x40x1	555714
D4	170000 Core: 250x40x15 Single face-sheet: 250x40x1	555714

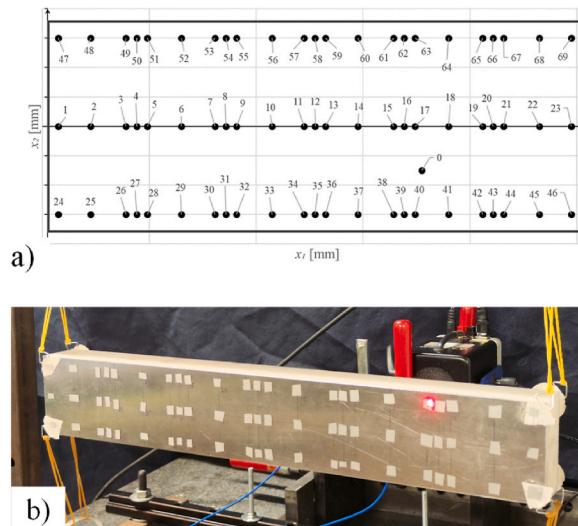


Fig. 7. A) Schematic representation of the scanned points in the (x_1, x_2) plane; b) Scanned points on one of the beam specimens.

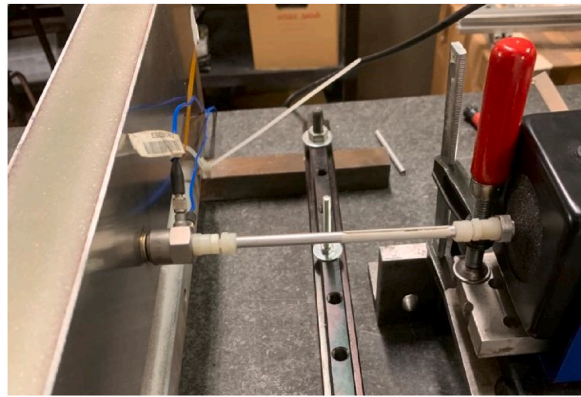


Fig. 8. Impedance head and shaker stinger.

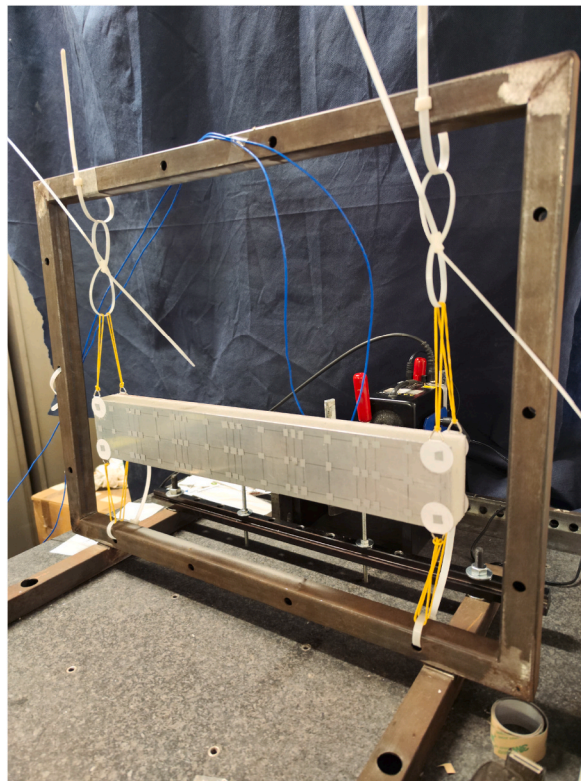


Fig. 9. Experimental set-up for the experimental modal analysis of the sandwich beams.

Table 7

CPU times (values are reported in seconds) and speedup for each sandwich model.

Specimen ID	MSC-NASTRAN	MATLAB® 2B-RZT ^(m) _(3.2)	Speedup
D1	516.0	15.5	33
D2	631.1	15.7	40
D3	602.4	16.2	37
D4	545.3	15.1	36

obtained with the high-fidelity 3D MSC-NASTRAN model. The differences observed between the numerical and experimental results might be related to the experimental part of the study.

5.4. Sensitivity to experimental variability: material property, constraints and torsional behaviour

In this section, the sensitivity of the proposed model with respect to some aspects of the experimental variability is assessed. In fact, the uncertainty on the material property of the core layer, in particular the shear modulus and the real applied boundary conditions, may significantly influence the numerical results. Additionally, the role of torsional-bending coupling observed experimentally is investigated. For a proper and clearer comparison, each of the assumed effects is addressed individually.

5.4.1. Sensitivity to the transverse shear property of the core layer

The transverse shear modulus of the WF110 core, i.e. the G value reported in Table 5, has been determined experimentally using a procedure based on a three-point bending test on the sandwich beam D1, as detailed in Ref. [57]. However, the value obtained under static test conditions might differ from those observed for dynamic responses; for example, different Rohacell® foams exhibit a stiffening effect at higher strain rates, as reported in Ref. [60]. In order to investigate this aspect further, a sensitivity analysis of the numerical results from 3D MSC-NASTRAN and $2B - RZT_{\{3,2\}}^{(m)}$ models is conducted. Specifically, considering the greater uncertainties in retrieving the shear modulus value, compared to the Young's modulus, of the WF110 foam highlighted in Ref. [57], a variation of $\pm 15\%$ w.r.t. the reference value reported in Table 5 has been taken into account. Table 12 reports the percentage variations of the first five frequencies for sandwich D1, relative to those obtained using the reference G value of Table 5. This sensitivity analysis is limited to the sandwich beam D1, which was the subject of the previous study aimed at evaluating the shear modulus of the WF110.

Generally, as shown in Table 12 and for both numerical models, a 5% variation in the shear modulus G results in a corresponding variation of approximately 1.5%–2% in the frequencies. In this regard, both numerical models demonstrate a similar sensitivity to variations of the shear material stiffness, which confirms the accuracy of the transverse shear predictions of the $RZT_{\{3,2\}}^{(m)}$ formulation. Moreover, from Tables 12 and it is observed that for a positive variation of the shear modulus, i.e. +15%, a corresponding increase of the frequency is obtained for all of the considered modal shapes, reducing the discrepancy between the numerical and the experimental results. Similar results are expected also for the other sandwich beam configurations. Clearly, a variation of 15% of the WF110 shear modulus is considerably large, especially considering that all the frequencies are below 3 kHz. However, this variation might contribute as a possible explanation of the stiffening effect observed in the experimental data.

5.4.2. Sensitivity to the boundary conditions

The numerical vs experimental differences can also be interpreted by considering that both numerical models assume ideal free-free boundary conditions, which do not completely correspond to the experimental set-up. The cable ties and rubber bands (although with mechanical properties quite lower with respect to those of the materials used for the beams) contribute to increasing the experimental frequencies by adding more complex constraint conditions. Moreover, the loading conditions also lead to an increased stiffness of the experimental set-up. In fact, the force application area is a circular surface of 10 mm in diameter, which constrains the displacements of that point.

In order to address the first of these two potential sources of numerical vs experimental discrepancies, Table 13 shows the numerical results obtained with the $2B - RZT_{\{3,2\}}^{(m)}$ FE model in which only the bending rotation, i.e. the θ dof around the x_2 - axis, has been constrained on both beam edges. These modified boundary conditions aim to simulate the effect of the rubber bands that limit the axial displacement on the top and bottom external beam surfaces. No additional constraint conditions are enforced on the remaining dofs on the beam edges, i.e. $u, w^{(0)}, w^{(1)}$ and $w^{(2)}$.

As it can be seen, the effect of the modified boundary conditions, more similar to those observed in the experimental set-up, is to increase the stiffness of the numerical models. For some frequencies, the observed errors w.r.t. the experimental results are lower than 5%. Clearly, the rubber bands' pre-tensioning and the shaker's stinger are expected to provide a similar influence on the sandwich numerical model stiffness.

5.4.3. Experimental beam torsional behaviour

A further effect that may contribute to explaining the differences between the numerical and experimental results is the torsional-flexural coupling observed in some of the experimental modal shapes. Since the current version of the beam $RZT_{\{3,2\}}^{(m)}$ formulation does not include the torsional behaviour, the comparison in this case is made between the experimental results and the 3D MSC-NASTRAN predictions.

As an example, we focus our attention on the experimental modal shapes of the first fundamental frequency for the four sandwich beams considered in this study. Their shapes are represented in Fig. 10. Although these shapes are associated mainly to a flexural mode, a torsional component is clearly present in all of them.

This phenomenon can be better understood by analyzing the experimental FRFs while taking into account the natural frequencies computed using the 3D MSC-NASTRAN model, in which bending and torsional modes are uncoupled. Considering the frequency range from 400 Hz to 1.2 kHz for the four sandwich beams, the first torsional (1 T) and the first flexural (1 F) frequencies predicted by MSC-NASTRAN are shown on the experimental FRFs of the scanning point 25 (for reference, see Fig. 7) in Fig. 11.

Firstly, it can be observed that the numerical values for the first torsional and flexural frequencies are very close to each other. For

Table 8

Experimental and numerical frequencies (in Hz) of the D1 sandwich beam (in brackets, the percent errors).

Mode	Experimental frequencies	Experimental damping factor	2B-RZT ^(m) _(3,2) frequencies	MSC-NASTRAN frequencies
1	764.95	0.68 %	703.67 (−8.0 %)	710.38 (−7.1 %)
2	1277.75	1.71 %	1148.85 (−10.1 %)	1162.99 (−9.0 %)
3	1859.23	1.68 %	1635.65 (−12.0 %)	1661.40 (−10.6 %)
4	2368.74	1.81 %	2050.93 (−13.4 %)	2091.40 (−11.7 %)
5	2881.96	2.19 %	2514.79 (−12.7 %)	2577.60 (−10.6 %)

Table 9

Experimental and numerical frequencies (in Hz) of the D2 sandwich beam (in brackets, the percent errors).

Mode	Experimental frequencies	Experimental damping factor	2B-RZT ^(m) _(3,2) frequencies	MSC-NASTRAN frequencies
1	794.30	1.15 %	734.12 (−7.6 %)	747.92 (−5.8 %)
2	1434.06	1.66 %	1309.77 (−8.7 %)	1337.60 (−6.7 %)
3	2120.12	1.84 %	1894.03 (−10.7 %)	1938.30 (−8.6 %)
4	2768.03	1.94 %	2416.09 (−12.7 %)	2479.50 (−10.4 %)
5	3315.51	1.92 %	2956.34 (−10.8 %)	3043.50 (−8.2 %)

Table 10

Experimental and numerical frequencies (in Hz) of the D3 sandwich beam (in brackets, the percent errors).

Mode	Experimental frequencies	Experimental damping factor	2B-RZT ^(m) _(3,2) frequencies	MSC-NASTRAN frequencies
1	662.34	0.84 %	610.60 (−7.8 %)	614.72 (−7.2 %)
2	1160.15	1.57 %	1035.37 (−10.8 %)	1044.80 (−9.9 %)
3	1688.45	2.08 %	1484.22 (−12.1 %)	1501.50 (−11.1 %)
4	2198.60	1.54 %	1885.44 (−14.2 %)	1913.20 (−13.0 %)
5	2659.24	1.87 %	2316.86 (−12.9 %)	2359.40 (−11.3 %)

instance, in sandwich beam D1, the difference is only 17 Hz, whereas for D4, it reaches nearly 200 Hz. Secondly, the experimental peaks in the FRFs that have contributed to determining the modal shapes represented in Fig. 10 are located very close to the values of flexural and torsional modes. While it is straightforward to distinguish the torsional and bending modes in the numerical case, it becomes very difficult to separate each contribution from an experimental point of view. As a consequence, the torsional and flexural modes can mutually influence one another, resulting in a frequency shift that cannot be captured by the numerical models.

Although these considerations have been made upon the 3D MSC-NASTRAN results, these findings are generally valid for any

Table 11

Experimental and numerical frequencies (in Hz) of the D4 sandwich beam (in brackets, the percent errors).

Mode	Experimental frequencies	Experimental damping factor	2B-RZT ^(m) _(3,2) frequencies	MSC-NASTRAN frequencies
1	654.10	1.33 %	629.75 (−3.7 %)	641.07 (−2.0 %)
2	1287.40	1.42 %	1175.62 (−8.7 %)	1199.30 (−6.8 %)
3	1942.27	1.79 %	1721.04 (−11.4 %)	1758.80 (−9.4 %)
4	2568.28	1.97 %	2222.18 (−13.5 %)	2275.70 (−11.4 %)
5	3094.25	1.98 %	2727.28 (−11.9 %)	2799.40 (−9.5 %)

Table 12

Sensitivity analysis of the first five frequencies of sandwich beam D1 (expressed in percent variation) with respect to the variation of the transverse shear modulus (G) of the WF110 foam core.

	ΔG	Δf ₁	Δf ₂	Δf ₃	Δf ₄	Δf ₅
MSC-NASTRAN	−15	−5.0	−6.4	−6.1	−6.1	−5.4
	−10	−3.3	−4.3	−4.2	−4.3	−3.8
	−5	−1.6	−2.1	−2.1	−2.1	−1.9
	5	1.5	2.0	2.1	2.1	2.0
	10	3.1	4.1	4.1	4.2	4.0
2B-RZT ^(m) _(3,2)	15	4.5	6.0	6.1	6.2	6.0
	−15	−5.3	−6.8	−6.9	−7.1	−7.0
	−10	−3.5	−4.5	−4.6	−4.7	−4.6
	−5	−1.7	−2.2	−2.2	−2.3	−2.2
	5	1.6	2.1	2.1	2.2	2.2
	10	3.1	4.2	4.3	4.4	4.3
	15	4.5	6.2	6.3	6.5	6.4

numerical model, including the possible extension of the $RZT_{\{3,2\}}^{(m)}$ formulation with the inclusion of the torsional effect.

6. Conclusions

This work presents the dynamic formulation of a higher-order mixed model based on the Refined Zigzag Theory (RZT) for the free-vibration analysis of sandwich beams. The beam displacement field enhances the first-order axial kinematics with a third-order zigzag function and assumes a smeared parabolic function for the transverse displacement. The transverse normal and the transverse shear stresses are assumed as independent fields. By using the Hellinger-Reissner mixed variational statement, the equations of motion and consistent boundary conditions are derived. A simple and efficient beam finite element has been recalled to address the dynamic behaviour of sandwich beams. A numerical assessment is presented to highlight the proposed model’s accuracy in frequency estimation and element convergence behaviour.

It has been observed that the $RZT_{\{3,2\}}^{(m)}$ model and the corresponding $2B - RZT_{\{3,2\}}^{(m)}$ elements are generally accurate in frequency and modal estimations with respect to the 3D numerical solution for a wide range of cases. However, when the core is made of soft materials, non-negligible discrepancies are observable in higher modes. This is mainly due to the third-order zigzag function that cannot reproduce complex distributions typical of these modal shapes. However, the $RZT_{\{3,2\}}^{(m)}$ model achieves a good accuracy for the displacement in the external face-sheets.

An experimental campaign using the LASER Doppler Vibrometry (LDV) has been conducted to determine the modal parameters of a set of four sandwich beams of different thickness made in ERGAL face-sheets and Rohacell® WF110 rigid foam core. For each sandwich beam, a high-fidelity 3D FE model based on MSC-NASTRAN has been used for the experimental setup and the numerical comparisons with the experimental results and the $2B - RZT_{\{3,2\}}^{(m)}$ ones. A computational assessment has been presented to highlight the efficiency of the proposed $2B - RZT_{\{3,2\}}^{(m)}$ elements. It has been observed that the $2B - RZT_{\{3,2\}}^{(m)}$ models are able to reach an accurate solution, comparable to that of the high-fidelity MSC-NASTRAN models, from 33 to 40 times faster.

The results of the experimental tests presented here exhibit a stiffer behaviour with respect to the ones obtained using the $2B - RZT_{\{3,2\}}^{(m)}$ elements. Since the same behaviour has been confirmed by the high-fidelity 3D FE models, it can be concluded that the discrepancies are related to the experimental set-up considered in this study.

The effect of the experimental uncertainties has been finely addressed. Specifically, the sensitivity of the numerical models w.r.t. the variability of transverse shear modulus of the WF110 foam is investigated. It has been observed that a 15 % variation of its value with respect to the reference value leads to nearly 6 % of variation in the estimated frequency, bringing the numerical results closer to the experimental ones. A more realistic set of numerical boundary conditions has been investigated, demonstrating that the frequencies are strongly influenced by the constraint mechanism. Finally, the effect of the torsional-bending coupling behaviour has been investigated as a possible reason for the frequency shifting and discrepancies between the numerical and experimental results.

In conclusion, the proposed mixed-RZT formulation provides a promising and computationally efficient tool for the dynamic analysis of thick sandwich beams. Furthermore, possible future perspectives might be to extend the mixed-RZT model to better account for soft-core behaviour, providing more accurate predictions of the sandwich structural response, damaged layers, viscoelastic effects, and extending the FE formulation to plate/shell problems.

CRedit authorship contribution statement

Matteo Sorrenti: Writing – original draft, Visualization, Validation, Software, Methodology, Investigation, Data curation, Conceptualization. **Marco Gherlone:** Writing – review & editing, Visualization, Validation, Supervision, Resources, Project administration, Funding acquisition, Formal analysis.

Declaration of competing interest

The authors declare that they have no known competing financial interests or personal relationships that could have appeared to influence the work reported in this paper.

Table 13

Natural flexural frequencies and percent errors with respect to the experimental results for beams D1-D4, with bending rotations constrained at both ends.

Mode	D1		D2		D3		D4	
	f [Hz]	% err	f [Hz]	% err	f [Hz]	% err	f [Hz]	% err
1	783.36	2.4	849.99	7.0	701.28	5.9	768.07	17.4
2	1238.46	-3.1	1411.51	-1.6	1123.35	-3.2	1290.16	0.2
3	1684.67	-9.4	1959.74	-7.6	1538.71	-8.9	1800.87	-7.3
4	2124.44	-10.3	2489.43	-10.1	1951.40	-11.2	2298.67	-10.5
5	2561.16	-11.1	3011.28	-9.2	2365.11	-11.1	2788.64	-9.9

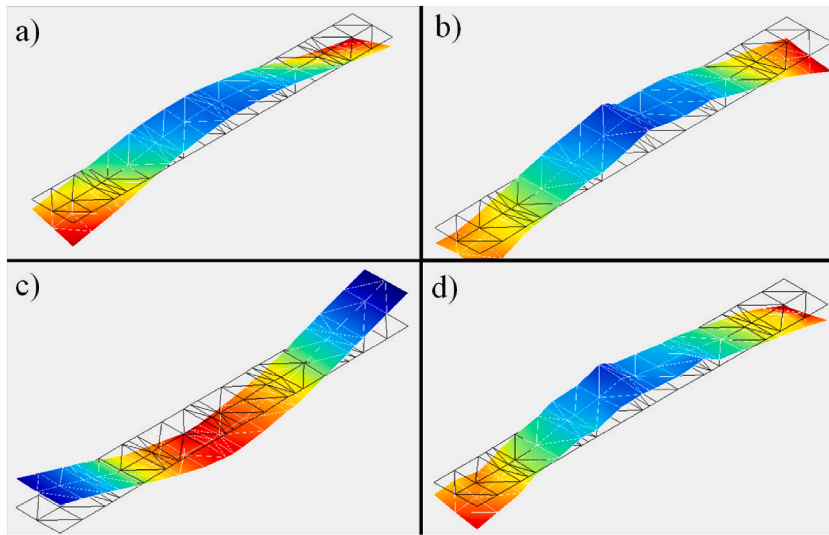


Fig. 10. Experimental modal shapes of the first fundamental frequency for sandwich beams: a) D1, b) D2, c) D3 and d) D4.

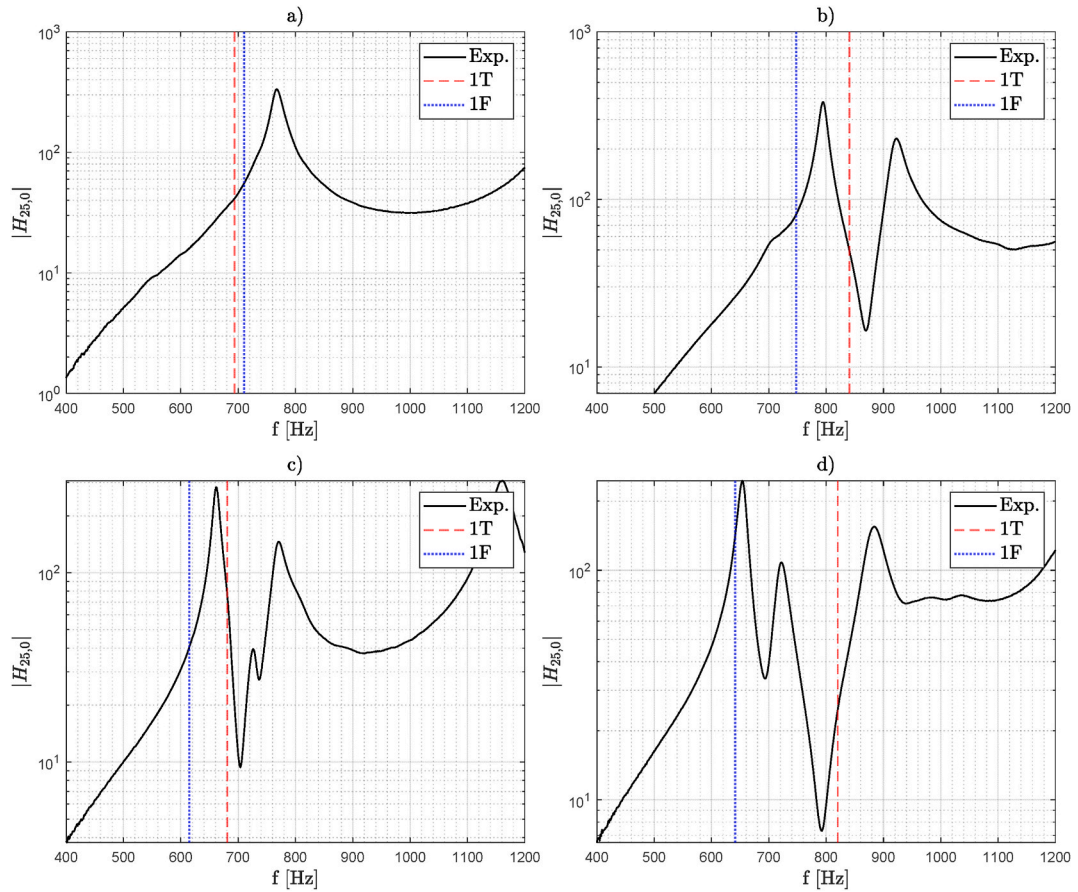


Fig. 11. Comparison of experimental FRF for point 25 of the sandwich beams a) D1, b) D2, c) D3, and d) D4) with the frequency values of the 3D MSC-NASTRAN models for the first flexural mode (1 F) and the first torsional mode (1 T).

Acknowledgments

The authors would like to thank Proff. Daniela Rigamonti and Paolo Bettini of the Department of Aerospace Sciences and Technologies – DAER (Politecnico di Milano) for their experience in the sandwich beam manufacturing process.

The authors acknowledge Simão Pedro Lima Carvalho for the support in the experimental set-up realization and experimental campaign.

Appendix A

Definition of auxiliary quantities.

For simplicity, some definitions and quantities used in the main body of the article are reported here.

In the definition of the transverse normal stress, see Eq. (17), the through-the-thickness functions are defined as follows

$$\begin{aligned}
 A_\sigma^u(x_3) &= \mathbf{P}_\sigma \langle S_{33}^{(k)} \mathbf{P}_\sigma^T \mathbf{P}_\sigma \rangle^{-1} \langle \mathbf{P}_\sigma^T \nu_{13}^{(k)} \rangle; \\
 A_\sigma^\theta(x_3) &= \mathbf{P}_\sigma \langle S_{33}^{(k)} \mathbf{P}_\sigma^T \mathbf{P}_\sigma \rangle^{-1} \langle \mathbf{P}_\sigma^T \nu_{13}^{(k)} x_3 \rangle; \\
 A_\sigma^\psi(x_3) &= \mathbf{P}_\sigma \langle S_{33}^{(k)} \mathbf{P}_\sigma^T \mathbf{P}_\sigma \rangle^{-1} \langle \mathbf{P}_\sigma^T \nu_{13}^{(k)} \mu^{(k)} \rangle; \\
 A_\sigma^w(x_3) &= \mathbf{P}_\sigma \langle S_{33}^{(k)} \mathbf{P}_\sigma^T \mathbf{P}_\sigma \rangle^{-1} \langle \mathbf{P}_\sigma^T \mathbf{H}_{,3} \rangle
 \end{aligned} \tag{A.1}$$

The quantities that appear in the RZT_{3,2}^(m) beam constitutive relations read:

$$\begin{aligned}
 \tilde{\mathbf{A}} &= \langle E_1^{(k)} + \nu_{13}^{(k)} A_\sigma^u \rangle; \quad \tilde{\mathbf{B}} = \langle x_3 E_1^{(k)} + \nu_{13}^{(k)} A_\sigma^\theta \rangle; \quad \tilde{\mathbf{A}}^\phi = \langle E_1^{(k)} \mu^{(k)} + \nu_{13}^{(k)} A_\sigma^\psi \rangle; \\
 \tilde{\mathbf{A}}^w &= \langle \nu_{13}^{(k)} A_\sigma^w \rangle; \quad \tilde{\mathbf{B}}^w = \langle x_3 \nu_{13}^{(k)} A_\sigma^w \rangle; \\
 \tilde{\mathbf{C}} &= \langle x_3 E_1^{(k)} + x_3 \nu_{13}^{(k)} A_\sigma^u \rangle; \quad \tilde{\mathbf{D}} = \langle x_3^2 E_1^{(k)} + x_3 \nu_{13}^{(k)} A_\sigma^\theta \rangle; \quad \tilde{\mathbf{B}}^\phi = \langle x_3 E_1^{(k)} \mu^{(k)} + x_3 \nu_{13}^{(k)} A_\sigma^\psi \rangle; \\
 \tilde{\mathbf{E}}^{\phi} &= \langle \mu^{(k)} E_1^{(k)} + \mu^{(k)} \nu_{13}^{(k)} A_\sigma^u \rangle; \quad \tilde{\mathbf{F}}^{\phi} = \langle x_3 \mu^{(k)} E_1^{(k)} + \mu^{(k)} \nu_{13}^{(k)} A_\sigma^\theta \rangle; \\
 \tilde{\mathbf{G}}^{\phi} &= \langle \mu^{(k)} E_1^{(k)} \mu^{(k)} + \mu^{(k)} \nu_{13}^{(k)} A_\sigma^u \rangle; \quad \tilde{\mathbf{C}}^w = \langle \mu^{(k)} \nu_{13}^{(k)} A_\sigma^w \rangle; \\
 \mathbf{A}^{Nz} &= \langle \mathbf{H}_{,3}^T A_\sigma^u \rangle; \quad \mathbf{B}^{Nz} = \langle \mathbf{H}_{,3}^T A_\sigma^\theta \rangle; \quad \mathbf{C}^{Nz} = \langle \mathbf{H}_{,3}^T A_\sigma^\psi \rangle; \quad \mathbf{D}^{Nz} = \langle \mathbf{H}_{,3}^T A_\sigma^w \rangle;
 \end{aligned} \tag{A.2}$$

Moreover, remembering that $S_t^{(k)} = 1/G_{13}^{(k)}$, the remaining quantities are expressed as follows:

$$\begin{aligned}
 \hat{\mathbf{A}}^w &= \langle \hat{\mathbf{A}}^z \mathbf{H}^z \rangle; \quad \hat{\mathbf{A}}^\theta = \langle \hat{\mathbf{A}}^z \rangle; \quad \hat{\mathbf{A}}^\psi = \langle \hat{\mathbf{A}}^z \mu_{,3}^{(k)} \rangle; \quad \hat{\mathbf{A}}^e = \langle \hat{\mathbf{A}}^z S_t^{(k)} \hat{\mathbf{A}}^z \rangle; \\
 \hat{\mathbf{A}}^k &= \langle \hat{\mathbf{A}}^z S_t^{(k)} \hat{\mathbf{B}}^z \rangle; \quad \hat{\mathbf{A}}^{k\psi} = \langle \hat{\mathbf{A}}^z S_t^{(k)} \hat{\mathbf{D}}^z \rangle; \quad \hat{\mathbf{A}}^{kw} = \langle \hat{\mathbf{A}}^z S_t^{(k)} \hat{\mathbf{E}}^z \rangle; \\
 \hat{\mathbf{B}}^w &= \langle \hat{\mathbf{B}}^z \mathbf{H}^z \rangle; \quad \hat{\mathbf{B}}^\theta = \langle \hat{\mathbf{B}}^z \rangle; \quad \hat{\mathbf{B}}^\psi = \langle \hat{\mathbf{B}}^z \mu_{,3}^{(k)} \rangle; \quad \hat{\mathbf{B}}^e = \hat{\mathbf{A}}^k = \langle \hat{\mathbf{B}}^z S_t^{(k)} \hat{\mathbf{A}}^z \rangle; \\
 \hat{\mathbf{B}}^k &= \langle \hat{\mathbf{B}}^z S_t^{(k)} \hat{\mathbf{B}}^z \rangle; \quad \hat{\mathbf{B}}^{k\psi} = \langle \hat{\mathbf{B}}^z S_t^{(k)} \hat{\mathbf{D}}^z \rangle; \quad \hat{\mathbf{B}}^{kw} = \langle \hat{\mathbf{B}}^z S_t^{(k)} \hat{\mathbf{E}}^z \rangle; \\
 \hat{\mathbf{C}}^w &= \langle \hat{\mathbf{D}}^z \mathbf{H}^z \rangle; \quad \hat{\mathbf{C}}^\theta = \langle \hat{\mathbf{D}}^z \rangle; \quad \hat{\mathbf{C}}^\psi = \langle \hat{\mathbf{D}}^z \mu_{,3}^{(k)} \rangle; \quad \hat{\mathbf{C}}^e = \hat{\mathbf{A}}^{k\psi} = \langle \hat{\mathbf{D}}^z S_t^{(k)} \hat{\mathbf{A}}^z \rangle; \\
 \hat{\mathbf{C}}^k &= \hat{\mathbf{B}}^{k\psi} = \langle \hat{\mathbf{D}}^z S_t^{(k)} \hat{\mathbf{B}}^z \rangle; \quad \hat{\mathbf{C}}^{k\psi} = \langle \hat{\mathbf{D}}^z S_t^{(k)} \hat{\mathbf{D}}^z \rangle; \quad \hat{\mathbf{C}}^{kw} = \langle \hat{\mathbf{D}}^z S_t^{(k)} \hat{\mathbf{E}}^z \rangle; \\
 \hat{\mathbf{D}}^w &= \langle \hat{\mathbf{E}}^z \mathbf{H}^z \rangle; \quad \hat{\mathbf{D}}^\theta = \langle \hat{\mathbf{E}}^z \rangle; \quad \hat{\mathbf{D}}^\psi = \langle \hat{\mathbf{E}}^z \mu_{,3}^{(k)} \rangle; \quad \hat{\mathbf{D}}^e = \hat{\mathbf{A}}^{kw} = \langle \hat{\mathbf{E}}^z S_t^{(k)} \hat{\mathbf{A}}^z \rangle; \\
 \hat{\mathbf{D}}^k &= \hat{\mathbf{B}}^{kw} = \langle \hat{\mathbf{E}}^z S_t^{(k)} \hat{\mathbf{B}}^z \rangle; \quad \hat{\mathbf{D}}^{k\psi} = \hat{\mathbf{C}}^{kw} = \langle \hat{\mathbf{E}}^z S_t^{(k)} \hat{\mathbf{D}}^z \rangle; \quad \hat{\mathbf{D}}^{kw} = \langle \hat{\mathbf{E}}^z S_t^{(k)} \hat{\mathbf{E}}^z \rangle;
 \end{aligned} \tag{A.3}$$

The through-the-thickness functions that appear in Eq. (A.2) and (A.3) and in the definition of the assumed transverse shear stress, see Eq. (19) follows:

$$\begin{aligned}
 \hat{\mathbf{A}}^z(x_3) &= \mathbf{A}^z(x_3) + \left(x_3 + h/2 \right) \frac{1}{h} \tilde{\mathbf{A}} \\
 \hat{\mathbf{B}}^z(x_3) &= \mathbf{B}^z(x_3) + \left(x_3 + h/2 \right) \frac{1}{h} \tilde{\mathbf{B}} \\
 \hat{\mathbf{D}}^z(x_3) &= \mathbf{D}^z(x_3) + \left(x_3 + h/2 \right) \frac{1}{h} \tilde{\mathbf{A}}^\phi \\
 \hat{\mathbf{E}}^z(x_3) &= \mathbf{E}^z(x_3) + \left(x_3 + h/2 \right) \frac{1}{h} \tilde{\mathbf{A}}^w \\
 \mathbf{Z}_t(x_3) &= \left[\hat{\mathbf{A}}^z(x_3) \quad \hat{\mathbf{B}}^z(x_3) \quad \hat{\mathbf{D}}^z(x_3) \quad \hat{\mathbf{E}}^z(x_3) \right]
 \end{aligned} \tag{A.4}$$

where

$$\begin{aligned}
 A^z(x_3) &= - \int_{-h/2}^{x_3} (E_1^{(k)} + \nu_{13}^{(k)} A_\sigma^u) dx_3 \\
 B^z(x_3) &= - \int_{-h/2}^{x_3} (x_3 E_1^{(k)} + \nu_{13}^{(k)} A_\sigma^\theta) dx_3 \\
 D^z(x_3) &= - \int_{-h/2}^{x_3} (E_1^{(k)} \mu^{(k)} + \nu_{13}^{(k)} A_\sigma^\psi) dz \\
 E^z(x_3) &= \left[\begin{aligned} & - \int_{-h/2}^{x_3} \nu_{13}^{(k)} A_{\sigma 11}^w dx_3 \\ & - \int_{-h/2}^{x_3} \nu_{13}^{(k)} A_{\sigma 12}^w dx_3 \\ & - \int_{-h/2}^{x_3} \nu_{13}^{(k)} A_{\sigma 13}^w dx_3 \end{aligned} \right]
 \end{aligned} \tag{A.5}$$

Finally, the remaining terms that appear in the governing equation and boundary conditions of the RZT_{3,2}^(m) model, see Eqs. (20) and (21), reads:

$$\widehat{Q}^{w0} = \widehat{A}_{11}^{kw} e_{,11} + \widehat{B}_{11}^{kw} k_{,11} + \widehat{C}_{11}^{kw} k_{,11}^\psi + \widehat{D}_{11}^{kw} w_{,11}^{(0)} + \widehat{D}_{12}^{kw} w_{,11}^{(1)} + \widehat{D}_{13}^{kw} w_{,11}^{(2)} - \left(\widehat{D}_{11}^w w_{,11}^{(0)} + \widehat{D}_{12}^w w_{,11}^{(1)} + \widehat{D}_{13}^w w_{,11}^{(2)} + \widehat{D}_{11}^\theta \theta_{,1} + \widehat{D}_{11}^\psi \psi_{,1} \right) \tag{A.6}$$

$$\widehat{Q}^{w1} = \widehat{A}_{12}^{kw} e_{,11} + \widehat{B}_{12}^{kw} k_{,11} + \widehat{C}_{12}^{kw} k_{,11}^\psi + \widehat{D}_{21}^{kw} w_{,11}^{(0)} + \widehat{D}_{22}^{kw} w_{,11}^{(1)} + \widehat{D}_{23}^{kw} w_{,11}^{(2)} - \left(\widehat{D}_{11}^w w_{,11}^{(0)} + \widehat{D}_{12}^w w_{,11}^{(1)} + \widehat{D}_{13}^w w_{,11}^{(2)} + \widehat{D}_{21}^\theta \theta_{,1} + \widehat{D}_{21}^\psi \psi_{,1} \right) \tag{A.7}$$

$$\widehat{Q}^{w2} = \widehat{A}_{13}^{kw} e_{,11} + \widehat{B}_{13}^{kw} k_{,11} + \widehat{C}_{13}^{kw} k_{,11}^\psi + \widehat{D}_{31}^{kw} w_{,11}^{(0)} + \widehat{D}_{32}^{kw} w_{,11}^{(1)} + \widehat{D}_{33}^{kw} w_{,11}^{(2)} - \left(\widehat{D}_{31}^w w_{,11}^{(0)} + \widehat{D}_{32}^w w_{,11}^{(1)} + \widehat{D}_{33}^w w_{,11}^{(2)} + \widehat{D}_{31}^\theta \theta_{,1} + \widehat{D}_{31}^\psi \psi_{,1} \right) \tag{A.8}$$

$$E^{HR} = \widehat{A}_{11}^w w_{,11}^{(0)} + \widehat{A}_{12}^w w_{,11}^{(1)} + \widehat{A}_{13}^w w_{,11}^{(2)} + \widehat{A}_{11}^\theta \theta_{,1} + \widehat{A}_{11}^\psi \psi_{,1} - \left(\widehat{A}_{11}^e e_{,11} + \widehat{A}_{11}^k k_{,11} + \widehat{A}_{11}^{k\psi} k_{,11}^\psi + \widehat{A}_{11}^{kw} w_{,11}^{(0)} + \widehat{A}_{12}^{kw} w_{,11}^{(1)} + \widehat{A}_{13}^{kw} w_{,11}^{(2)} \right) \tag{A.9}$$

$$K^{HR} = \widehat{B}_{11}^w w_{,11}^{(0)} + \widehat{B}_{12}^w w_{,11}^{(1)} + \widehat{B}_{13}^w w_{,11}^{(2)} + \widehat{B}_{11}^\theta \theta_{,1} + \widehat{B}_{11}^\psi \psi_{,1} - \left(\widehat{A}_{11}^k e_{,11} + \widehat{B}_{11}^k k_{,11} + \widehat{B}_{11}^{k\psi} k_{,11}^\psi + \widehat{B}_{11}^{kw} w_{,11}^{(0)} + \widehat{B}_{12}^{kw} w_{,11}^{(1)} + \widehat{B}_{13}^{kw} w_{,11}^{(2)} \right) \tag{A.10}$$

$$K_\psi^{HR} = \widehat{C}_{11}^w w_{,11}^{(0)} + \widehat{C}_{12}^w w_{,11}^{(1)} + \widehat{C}_{13}^w w_{,11}^{(2)} + \widehat{C}_{11}^\theta \theta_{,1} + \widehat{C}_{11}^\psi \psi_{,1} - \left(\widehat{A}_{11}^{k\psi} e_{,11} + \widehat{B}_{11}^{k\psi} k_{,11} + \widehat{C}_{11}^{k\psi} k_{,11}^\psi + \widehat{C}_{11}^{kw} w_{,11}^{(0)} + \widehat{C}_{12}^{kw} w_{,11}^{(1)} + \widehat{C}_{13}^{kw} w_{,11}^{(2)} \right) \tag{A.11}$$

$$\begin{aligned}
 \overset{HR}{E}^e &= \widehat{A}^w \partial w + \widehat{A}^\theta \theta + \widehat{A}^\psi \psi - \left(\widehat{A}^e e_{,1} + \widehat{A}^k k_{,1} + \widehat{A}^{k\psi} k_{,1}^\psi + \widehat{A}^{kw} \partial w \right) \\
 \overset{HR}{K}^k &= \widehat{B}^w \partial w + \widehat{B}^\theta \theta + \widehat{B}^\psi \psi - \left(\widehat{B}^e e_{,1} + \widehat{B}^k k_{,1} + \widehat{B}^{k\psi} k_{,1}^\psi + \widehat{B}^{kw} \partial w \right) \\
 \overset{HR}{K}^{k\psi} &= \widehat{C}^w \partial w + \widehat{C}^\theta \theta + \widehat{C}^\psi \psi - \left(\widehat{C}^e e_{,1} + \widehat{C}^k k_{,1} + \widehat{C}^{k\psi} k_{,1}^\psi + \widehat{C}^{kw} \partial w \right) \\
 \overset{HR}{Q} &= \left[\overset{HR}{Q}_1^{w0} \quad \overset{HR}{Q}_1^{w1} \quad \overset{HR}{Q}_1^{w2} \right] = \widehat{D}^w \partial w + \widehat{D}^\theta \theta + \widehat{D}^\psi \psi - \left(\widehat{A}^{kwT} e_{,1} + \widehat{B}^{kwT} k_{,1} + \widehat{C}^{kwT} k_{,1}^\psi + \widehat{D}^{kw} \partial w \right)
 \end{aligned} \tag{A.12}$$

Appendix B

Full expression of the elemental and mass matrices.

In this appendix, the full expression of the elemental stiffness and mass matrices that appear in Eq. (36) are briefly reported.

$$\mathbf{K}_{dd}^{(e)} = \int_{L^{(e)}} \begin{bmatrix} (\mathbf{L}_{,1}^T \tilde{\mathbf{A}} \mathbf{L}_{,1} + bh/\eta \mathbf{L}_{,1}^T \mathbf{L}_{,1}) & \mathbf{L}_{,1}^T \tilde{\mathbf{A}}^w \mathbf{L}^w & \mathbf{L}_{,1}^T \tilde{\mathbf{B}} \mathbf{L}_{,1} & \mathbf{L}_{,1}^T \tilde{\mathbf{A}}^\phi \mathbf{L}_{,1} \\ \mathbf{L}^{wT} \mathbf{A}^{Nz} \mathbf{L}_{,1} & (\mathbf{L}^{wT} \mathbf{D}^{Nz} \mathbf{L}^w + \mathbf{L}_{,1}^{wT} \widehat{\mathbf{D}}^{wT} \mathbf{L}_{,1}^w + \mathbf{L}_{,1}^{wT} \widehat{\mathbf{D}}^{kw} \mathbf{L}_{,1}^w - \mathbf{L}_{,1}^{wT} \widehat{\mathbf{D}}^{kw} \mathbf{L}_{,1}^w) & (\mathbf{L}^{wT} \mathbf{B}^{Nz} \mathbf{L}_{,1} + \mathbf{L}_{,1}^{wT} \widehat{\mathbf{D}}^\theta \mathbf{L}) & (\mathbf{L}^{wT} \mathbf{C}^{Nz} \mathbf{L}_{,1} + \mathbf{L}_{,1}^{wT} \widehat{\mathbf{D}}^\psi \mathbf{L}) \\ \mathbf{L}_{,1}^T \tilde{\mathbf{C}} \mathbf{L}_{,1} & \mathbf{L}^T \widehat{\mathbf{D}}^{\theta T} \mathbf{L}_{,1}^w + \mathbf{L}_{,1}^T \tilde{\mathbf{B}}^w \mathbf{L}^w & (\mathbf{L}_{,1}^T \tilde{\mathbf{D}} \mathbf{L}_{,1} + bh/\eta \mathbf{L}_{,1}^T \mathbf{L}_{,1}) & \mathbf{L}_{,1}^T \tilde{\mathbf{B}}^\phi \mathbf{L}_{,1} \\ \mathbf{L}_{,1}^T \tilde{\mathbf{E}}^\phi \mathbf{L}_{,1} & \mathbf{L}^T \widehat{\mathbf{D}}^{\psi T} \mathbf{L}_{,1}^w + \mathbf{L}_{,1}^T \tilde{\mathbf{C}}^w \mathbf{L}^w & \mathbf{L}_{,1}^T \tilde{\mathbf{F}}^\phi \mathbf{L}_{,1} & (\mathbf{L}_{,1}^T \tilde{\mathbf{G}}^\phi \mathbf{L}_{,1} + bh/\eta \mathbf{L}_{,1}^T \mathbf{L}_{,1}) \end{bmatrix} dx_1 \tag{B.1}$$

$$\mathbf{K}_{de}^{(e)} = \mathbf{K}_{ed}^{(e)T} = \int_{L^{(e)}} \begin{bmatrix} -bh/\eta \mathbf{L}_{,1}^T \mathbf{L} & \mathbf{0} & \mathbf{0} \\ (\mathbf{L}_{,1}^{wT} \widehat{\mathbf{A}}^{wT} \mathbf{L}_{,1} + \mathbf{L}_{,1}^{wT} \widehat{\mathbf{B}}^w \mathbf{L}_{,1} + \mathbf{L}_{,1}^{wT} \widehat{\mathbf{C}}^{wT} \mathbf{L}_{,1} - \mathbf{L}_{,1}^{wT} \widehat{\mathbf{D}}^e \mathbf{L}_{,1}) & (\mathbf{L}_{,1}^{wT} \widehat{\mathbf{B}}^k \mathbf{L}_{,1}) & (-\mathbf{L}_{,1}^{wT} \widehat{\mathbf{D}}^{kw} \mathbf{L}_{,1}) \\ \mathbf{L}^T \widehat{\mathbf{A}}^\theta \mathbf{L}_{,1} & (\mathbf{L}^T \widehat{\mathbf{B}}^\theta \mathbf{L}_{,1} + -bh/\eta \mathbf{L}_{,1}^T \mathbf{L}) & \mathbf{L}^T \widehat{\mathbf{C}}^\theta \mathbf{L}_{,1} \\ \mathbf{L}^T \widehat{\mathbf{A}}^\psi \mathbf{L}_{,1} & \mathbf{L}^T \widehat{\mathbf{B}}^\psi \mathbf{L}_{,1} & (\mathbf{L}^T \widehat{\mathbf{C}}^\psi \mathbf{L}_{,1} + -bh/\eta \mathbf{L}_{,1}^T \mathbf{L}) \end{bmatrix} dx_1 \tag{B.2}$$

$$\mathbf{K}_{ee}^{(e)} = \int_{L^{(e)}} \begin{bmatrix} -\mathbf{L}_{,1}^T \widehat{\mathbf{A}}^e \mathbf{L}_{,1} + bh/\eta \mathbf{L}^T \mathbf{L} & -\mathbf{L}_{,1}^T \widehat{\mathbf{A}}^k \mathbf{L}_{,1} & -\mathbf{L}_{,1}^T \widehat{\mathbf{A}}^{kw} \mathbf{L}_{,1} \\ -\mathbf{L}_{,1}^T \widehat{\mathbf{B}}^e \mathbf{L}_{,1} & -\mathbf{L}_{,1}^T \widehat{\mathbf{B}}^k \mathbf{L}_{,1} + bh/\eta \mathbf{L}^T \mathbf{L} & -\mathbf{L}_{,1}^T \widehat{\mathbf{B}}^{kw} \mathbf{L}_{,1} \\ -\mathbf{L}_{,1}^T \widehat{\mathbf{C}}^e \mathbf{L}_{,1} & -\mathbf{L}_{,1}^T \widehat{\mathbf{C}}^k \mathbf{L}_{,1} & -\mathbf{L}_{,1}^T \widehat{\mathbf{C}}^{kw} \mathbf{L}_{,1} + bh/\eta \mathbf{L}^T \mathbf{L} \end{bmatrix} dx_1 \tag{B.3}$$

$$\mathbf{M}_{dd}^{(e)} = \int_{L^{(e)}} \begin{bmatrix} m^{(0)} \mathbf{L}^T \mathbf{L} & \mathbf{0} & \mathbf{0} & \mathbf{0} & m^{(1)} \mathbf{L}^T \mathbf{L} & m_\mu^{(0)} \mathbf{L}^T \mathbf{L} \\ & m^{(0)} \mathbf{L}^T \mathbf{L} & m^{(1)} \mathbf{L}^T \mathbf{L} & m^{(2)} \mathbf{L}^T \mathbf{L} & \mathbf{0} & \mathbf{0} \\ & & m^{(2)} \mathbf{L}^T \mathbf{L} & m^{(3)} \mathbf{L}^T \mathbf{L} & \mathbf{0} & \mathbf{0} \\ & & & m^{(4)} \mathbf{L}^T \mathbf{L} & \mathbf{0} & \mathbf{0} \\ sym. & & & & m^{(2)} \mathbf{L}^T \mathbf{L} & m_\mu^{(1)} \mathbf{L}^T \mathbf{L} \\ & & & & & m_\mu^{(2)} \mathbf{L}^T \mathbf{L} \end{bmatrix} dx_1 \tag{B.4}$$

Data availability

Data will be made available on request.

References

[1] V. Birman, G.A. Kardomateas, Review of current trends in research and applications of sandwich structures, *Compos. B Eng.* 142 (2018) 221–240, <https://doi.org/10.1016/j.compositesb.2018.01.027>.

- [2] L.A. Carlsson, G.A. Kardomateas, *Structural and Failure Mechanics of Sandwich Composites*, first ed., Springer, Dordrecht, Heidelberg London New York, 2011. <https://link.springer.com/book/10.1007/978-1-4020-3225-7>.
- [3] M.F. Caliri, A.J.M. Ferreira, V. Tita, A review on plate and shell theories for laminated and sandwich structures highlighting the finite element method, *Compos. Struct.* 156 (2016) 63–77, <https://doi.org/10.1016/j.compstruct.2016.02.036>.
- [4] S. Abrate, M. Di Sciuva, Multilayer models for composite and sandwich structures, in: P.W.R. Beaumont, C.H. Zweben (Eds.), *Comprehensive Composite Materials II*, Elsevier, 2018, pp. 399–425, <https://doi.org/10.1016/B978-0-12-803581-8.09885-4>.
- [5] N.J. Pagano, Exact solutions for rectangular bidirectional composites and sandwich plates, *J. Compos. Mater.* 4 (1970) 20–34, <https://doi.org/10.1177/002199837000400102>.
- [6] S. Brischetto, An exact 3d solution for free vibrations of multilayered cross-ply composite and sandwich plates and shells, *Int. J. Appl. Mechanics* 6 (2014) 1450076, <https://doi.org/10.1142/S1758825114500768>.
- [7] P.R. Heyliger, J.N. Reddy, A higher order beam finite element for bending and vibration problems, *J. Sound Vib.* 126 (1988) 309–326, [https://doi.org/10.1016/0022-460X\(88\)90244-1](https://doi.org/10.1016/0022-460X(88)90244-1).
- [8] Y. Hilali, M. Rassam, S. Mesmoudi, Y. Sitli, O. Elmhaia, M. Rammane, O. Askour, O. Bourihane, A high-order approach for thermal buckling and post-buckling analysis of functionally graded sandwich beams, *Acta Mech.* 236 (2025) 3543–3563, <https://doi.org/10.1007/s00707-025-04342-5>.
- [9] Y. Hilali, Y. Sitli, O. Elmhaia, O. Askour, M. Rammane, S. Mesmoudi, O. Bourihane, An improved high-order kirigating mesh-free approach for nonlinear thermal buckling of porous FG beams, *Acta Mech.* 236 (2025) 2149–2169, <https://doi.org/10.1007/s00707-025-04252-6>.
- [10] S. Zghal, A. Frikha, F. Dammak, Free vibration analysis of carbon nanotube-reinforced functionally graded composite shell structures, *Appl. Math. Model.* 53 (2018) 132–155, <https://doi.org/10.1016/j.apm.2017.08.021>.
- [11] S. Zghal, A. Frikha, F. Dammak, Non-linear bending analysis of nanocomposites reinforced by graphene-nanotubes with finite shell element and membrane enhancement, *Eng. Struct.* 158 (2018) 95–109, <https://doi.org/10.1016/j.engstruct.2017.12.017>.
- [12] S. Zghal, S. Trabelsi, F. Dammak, Post-buckling behavior of functionally graded and carbon-nanotubes based structures with different mechanical loadings, *Mech. Base. Des. Struct. Mach.* 50 (2022) 2997–3039, <https://doi.org/10.1080/15397734.2020.1790387>.
- [13] N.J. Hoff, S.E. Mautner, Bending and buckling of sandwich beams, *J. Aeronaut. Sci.* 15 (1948) 707–720, <https://doi.org/10.2514/8.11699>.
- [14] E.M. Kerwin, Damping of flexural waves by a constrained viscoelastic layer, *J. Acoust. Soc. Am.* 31 (1959) 952–962, <https://doi.org/10.1121/1.1907821>.
- [15] R.A. DiTaranto, Theory of vibratory bending for elastic and viscoelastic layered finite-length beams, *J. Appl. Mech.* 32 (1965) 881–886, <https://doi.org/10.1115/1.3627330>.
- [16] D.J. Mead, S. Markus, The forced vibration of a three-layer, damped sandwich beam with arbitrary boundary conditions, *J. Sound Vib.* 10 (1969) 163–175, [https://doi.org/10.1016/0022-460X\(69\)90193-X](https://doi.org/10.1016/0022-460X(69)90193-X).
- [17] Y. Frostig, M. Baruch, O. Vilnay, I. Sheinman, High-order theory for sandwich-beam behavior with transversely flexible core, *J. Eng. Mech.* 118 (1992) 1026–1043, [https://doi.org/10.1061/\(ASCE\)0733-9399\(1992\)118:51026](https://doi.org/10.1061/(ASCE)0733-9399(1992)118:51026).
- [18] S. Abrate, M. Di Sciuva, Equivalent single layer theories for composite and sandwich structures: a review, *Compos. Struct.* 179 (2017) 482–494, <https://doi.org/10.1016/j.compstruct.2017.07.090>.
- [19] A.S. Sayyad, Y.M. Ghugal, Bending, buckling and free vibration of laminated composite and sandwich beams: a critical review of literature, *Compos. Struct.* C (2017) 486–504, <https://doi.org/10.1016/j.compstruct.2017.03.053>.
- [20] D. Li, Layerwise theories of laminated composite structures and their applications: a review, *Arch Computat Methods Eng* 28 (2021) 577–600, <https://doi.org/10.1007/s11831-019-09392-2>.
- [21] M. Di Sciuva, Development of an anisotropic, multilayered, shear-deformable rectangular plate element, *Comput. Struct.* 21 (1985) 789–796, [https://doi.org/10.1016/0045-7949\(85\)90155-5](https://doi.org/10.1016/0045-7949(85)90155-5).
- [22] M. Di Sciuva, U. Icardi, Analysis of thick multilayered anisotropic plates by a higher order plate element, *AIAA J.* 33 (1995) 2435–2437, <https://doi.org/10.2514/3.13009>.
- [23] M. Di Sciuva, Geometrically nonlinear theory of multilayered plates with interlayer slips, *AIAA J.* 35 (1997) 1753–1759, <https://doi.org/10.2514/2.23>.
- [24] A. Tessler, M. Di Sciuva, M. Gherlone, Refinement of Timoshenko Beam Theory for Composite and Sandwich Beams Using Zigzag Kinematics, *NASA/TP-2007-215086*, 2007, pp. 1–45. <https://ntrs.nasa.gov/citations/20070035078>.
- [25] M. Gherlone, A. Tessler, M. Di Sciuva, C⁰ beam elements based on the refined zigzag theory for multilayered composite and sandwich laminates, *Compos. Struct.* 93 (2011) 2882–2894, <https://doi.org/10.1016/j.compstruct.2011.05.015>.
- [26] E. Oñate, A. Eijo, S. Oller, Simple and accurate two-noded beam element for composite laminated beams using a refined zigzag theory, *Comput. Methods Appl. Mech. Eng.* (2012) 213–216, <https://doi.org/10.1016/j.cma.2011.11.023>, 362–382.
- [27] A. Ascione, A.C. Orifici, M. Gherlone, Experimental and numerical investigation of the refined zigzag theory for accurate buckling analysis of highly heterogeneous sandwich beams, *Int. J. Str. Stab. Dyn.* 20 (2020) 1–27, <https://doi.org/10.1142/S0219455420050789>.
- [28] L. Iurlaro, A. Ascione, M. Gherlone, M. Mattone, M. Di Sciuva, Free vibration analysis of sandwich beams using the refined zigzag theory: an experimental assessment, *Meccanica* 50 (2015) 2525–2535, <https://doi.org/10.1007/s11012-015-0166-4>.
- [29] L. Iurlaro, M. Gherlone, M. Mattone, M. Di Sciuva, Experimental assessment of the refined zigzag theory for the static bending analysis of sandwich beams, *Jnl of Sandwich Structures & Materials* 20 (2018) 86–105, <https://doi.org/10.1177/1099636216650614>.
- [30] H. Wimmer, W. Hochhauser, K. Nachbagaer, Refined zigzag theory: an appropriate tool for the analysis of CLT-Plates and other shear-elastic timber structures, *Eur. J. Wood Prod.* 78 (2020) 1125–1135, <https://doi.org/10.1007/s00107-020-01586-x>.
- [31] H. Wimmer, C. Celigoi, W. Hochhauser, A new approach for buckling analysis of laminated glass panels, *AIP Conf. Proc.* 2928 (2023) 150030, <https://doi.org/10.1063/5.0170901>.
- [32] A. Kefal, K.A. Hasim, M. Yildiz, A novel isogeometric beam element based on mixed form of refined zigzag theory for thick sandwich and multilayered composite beams, *Compos. B Eng.* 167 (2019) 100–121, <https://doi.org/10.1016/j.compositesb.2018.11.102>.
- [33] M. Ermis, M. Dorduncu, A. Kutlu, Peridynamic differential operator for stress analysis of imperfect functionally graded porous sandwich beams based on refined zigzag theory, *Appl. Math. Model.* (2024), <https://doi.org/10.1016/j.apm.2024.05.032>.
- [34] P. Cerracchio, M. Gherlone, M. Di Sciuva, A. Tessler, A novel approach for displacement and stress monitoring of sandwich structures based on the inverse finite element method, *Compos. Struct.* 127 (2015) 69–76, <https://doi.org/10.1016/j.compstruct.2015.02.081>.
- [35] A. Kefal, I.E. Tabrizi, M. Yildiz, A. Tessler, A smoothed iFEM approach for efficient shape-sensing applications: numerical and experimental validation on composite structures, *Mech. Syst. Signal Process.* 152 (2021) 1–34, <https://doi.org/10.1016/j.ymsp.2020.107486>.
- [36] V.-H. Truong, Q.-H. Le, J. Lee, J.-W. Han, A. Tessler, S.-N. Nguyen, An efficient neural network approach for laminated composite plates using refined zigzag theory, *Compos. Struct.* 348 (2024) 118476, <https://doi.org/10.1016/j.compstruct.2024.118476>.
- [37] M. Ermis, M. Dorduncu, G. Aydogan, Physics-based machine learning for modeling of laminated composite plates based on refined zigzag theory, *Arch. Appl. Mech.* 95 (2025) 107, <https://doi.org/10.1007/s00419-025-02816-5>.
- [38] M. Sorrenti, M. Di Sciuva, An enhancement of the warping shear functions of refined zigzag theory, *J. Appl. Mech.* 88 (2021), <https://doi.org/10.1115/1.4050908>.
- [39] M. Di Sciuva, M. Sorrenti, New accomplishments on the equivalence of the first-order displacement-based zigzag theories through a unified formulation, *J. Compos. Sci.* 8 (2024) 181, <https://doi.org/10.3390/jcs8050181>.
- [40] M. Sorrenti, M. Gherlone, Robust TRIA3 and QUAD4 finite elements based on the En-RZT kinematics for the analysis of general anisotropic multilayered composite plates, *Mech. Compos. Mater.* 60 (2024) 1001–1026, <https://doi.org/10.1007/s11029-024-10241-y>.
- [41] S. de Miranda, L. Patruno, F. Ubertini, Transverse stress profiles reconstruction for finite element analysis of laminated plates, *Compos. Struct.* 94 (2012) 2706–2715, <https://doi.org/10.1016/j.compstruct.2012.03.026>.
- [42] P.M. Daniel, J. Främby, M. Fagerström, P. Maimí, Complete transverse stress recovery model for linear shell elements in arbitrarily curved laminates, *Compos. Struct.* 252 (2020) 112675, <https://doi.org/10.1016/j.compstruct.2020.112675>.

- [43] L. Iurlaro, M. Gherlone, M. Di Sciuva, The (3,2)-Mixed refined zigzag theory for generally laminated beams: theoretical development and C^0 finite element formulation, *Int. J. Solid Struct.* (2015) 73–74, <https://doi.org/10.1016/j.ijsolstr.2015.07.028>, 1–19.
- [44] R.M.J. Groh, P.M. Weaver, A computationally efficient 2D model for inherently equilibrated 3D stress predictions in heterogeneous laminated plates. Part I: model formulation, *Compos. Struct.* 156 (2016) 171–185, <https://doi.org/10.1016/j.compstruct.2015.11.078>.
- [45] R.M.J. Groh, P.M. Weaver, A computationally efficient 2D model for inherently equilibrated 3D stress predictions in heterogeneous laminated plates. Part II: model validation, *Compos. Struct.* 156 (2016) 186–217, <https://doi.org/10.1016/j.compstruct.2015.11.077>.
- [46] A. Kutlu, Mixed finite element formulation for bending of laminated beams using the refined zigzag theory, *Proc. Inst. Mech. Eng., Part L* 235 (2021) 1712–1722, <https://doi.org/10.1177/14644207211018839>.
- [47] K. Washizu, *Variational Methods in Elasticity and Plasticity*, Second, Pergamon Press, 1974.
- [48] S. Zghal, F. Dammak, Vibrational behavior of beams made of functionally graded materials by using a mixed formulation, *Proc. IME C J. Mech. Eng. Sci.* 234 (2020) 3650–3666, <https://doi.org/10.1177/0954406220916533>.
- [49] L.C. Trinh, S.O. Ojo, R.M.J. Groh, P.M. Weaver, A mixed inverse differential quadrature method for static analysis of constant- and variable-stiffness laminated beams based on hellinger-reissner mixed variational formulation, *Int. J. Solid Struct.* (2021) 210–211, <https://doi.org/10.1016/j.ijsolstr.2020.11.019>, 66–87.
- [50] M. Sorrenti, M. Gherlone, A new mixed model based on the enhanced-Refined zigzag theory for the analysis of thick multilayered composite plates, *Compos. Struct.* 311 (2023) 116787, <https://doi.org/10.1016/j.compstruct.2023.116787>.
- [51] M. Sorrenti, M. Gherlone, Numerical and experimental predictions of the static behaviour of thick sandwich beams using a mixed {3,2}-RZT formulation, *Finite Elem. Anal. Des.* 242 (2024) 1–31, <https://doi.org/10.1016/j.finela.2024.104267>.
- [52] M. Di Sciuva, M. Gherlone, A global/local third-order Hermitian displacement field with damaged interfaces and transverse extensibility: analytical formulation, *Compos. Struct.* 59 (2003) 419–431, [https://doi.org/10.1016/S0263-8223\(02\)00168-X](https://doi.org/10.1016/S0263-8223(02)00168-X).
- [53] I. Babuška, The finite element method with Lagrangian multipliers, *Numer. Math.* 20 (1973) 179–192, <https://doi.org/10.1007/BF01436561>.
- [54] F. Brezzi, On the existence, uniqueness and approximation of saddle-point problems arising from lagrangian multipliers, *R.A.I.R.O. analyse, Numérique* 8 (1974) 129–151, <https://doi.org/10.1051/m2an/197408R201291>.
- [55] Reference Guide - MSC Nastran 2021, 2020.
- [56] 3M Scotch-Weld Structural Adhesive Film AF 163-2, 3M Aerospace and Aircraft Maintenance Department, St. Paul, MN, 2009.
- [57] M. Sorrenti, Refined Zigzag Models for the Response of General Multilayered Composite and Sandwich Structures: Numerical and Experimental Investigations, PhD Thesis, Politecnico di Torino, 2023. <https://iris.polito.it/handle/11583/2981462?mode=simple>.
- [58] Modal testing: a practical guide, (n.d.). <https://community.sw.siemens.com/s/article/Modal-Testing-A-Guide>.
- [59] Getting started with modal curvefitting, (n.d.). <https://community.sw.siemens.com/s/article/getting-started-with-modal-curvefitting>.
- [60] S. Poxon, The Mechanical Response of Low to High Density Rohacell Foams, PhD Thesis, Oxford University UK, 2013. <https://ora.ox.ac.uk/objects/uuid:94065572-8e3c-4e68-8e40-12f148093717>.